Phase matrix characterization of long-range transported Saharan dust using multiwavelength polarized polar imaging nephelometry

Elena Bazo[1,2], Daniel Pérez-Ramírez[1,2], Antonio Valenzuela[1,2], J. Vanderlei Martins[3], Gloria Titos[1,2], Alberto Cazorla[1,2], Fernando Rejano[4], Diego Patrón[1,2], Arlett Díaz-Zurita[1,2], Francisco José García-Izquierdo[1,4], David Fuertes[5], Lucas Alados-Arboledas[1,2] and Francisco José Olmo[1,2]

[1]Andalusian Institute for Earth System Research (IISTA-CEAMA), Granada 18006, Spain

[2]Department of Applied Physics, University of Granada, Granada 18071, Spain

[3]JDepartment of Physics and Earth and Space Institute, University of Maryland Baltimore County, Baltimore, Maryland, USA

[4]Instituto de Astrofísica de Andalucía (IAA-CSIC), Granada 18008

[5]GRASP-SAS, Remote Sensing Developments, LOA/Université de Lille-1, 59655, Villeneuve, D'Ascq, France

Correspondence to: Daniel Pérez-Ramírez (dperez@ugr.es)

Abstract. This work investigates the scattering matrix elements during different Saharan dust outbreaks over Granada (South-East Spain) in 2022 using the Polarized Imaging Nephelometer (PI-Neph PIN100, GRASP-Earth). The PI-Neph is a unique instrument capable of measuring continuously the phase function and polarized phase function (F_{11} and $-F_{12}/F_{11}$) at three different wavelengths (405, 515 and 660 nm) with 1° resolution. Extreme dust events (PM_{10} concentration above 1000 µgm^{-3}) occurring in March 2022 are compared with more frequent and moderate events registered in summer 2022 (PM_{10} concentration between 50 and 100 µgm^{-3}). For F_{11} there are no remarkable differences between extreme and moderate events. However, results of $-F_{12}/F_{11}$ show large differences between extreme and moderate events, especially for the 405 nm wavelength. These differences are also observed when studying the temporal evolutions during the extreme events and reveal that $-F_{12}/F_{11}$ patterns similar to laboratory measurements occurred during the more intense periods of dust influence. Other aerosol optical properties were derived from the PI-Neph, such as the asymmetry parameter (g), the fraction of backscattered light (Bs) and the lidar ratio (LR). In general, g and Bs show typical values (g > 0.65 and Bs ~ 0.1) for both extreme and moderate Saharan dust events. However, the LR shows more variable values for the different dust events, ranging from 20 to 60 sr^{-1}. The combination with additional in-situ instrumentation allowed to obtain scattering (SAE) and absorption (AAE) Ångström exponents and to conduct a typing classification that revealed extreme dust events as pure dust while moderate dust events were classified as a mixture of dust with urban background pollution. In addition, model simulations with the Generalized Retrieval of Atmosphere and Surface Properties (GRASP) code reproduce well the PI-Neph measurements. Therefore, our results confirm that differences in the phase matrix elements of Saharan dust outbreaks of varying intensity can be explained by the mixing conditions of dust with the background particles, which varies from almost pure dust particles during extreme events, to a mixture of dust with local pollution during moderate events.

1 Introduction

The imprecise determination of atmospheric aerosol microphysical properties is currently the main source of uncertainty in climate projections, as stated by the latest Intergovernmental Panel on Climate Change (IPCC – Forster et al., (2021)). Particularly, aerosol particles can scatter and absorb solar radiation, known as the direct effect (Haywood et al., 2000). Moreover, aerosol particles can interact with clouds in different ways: aerosol absorption can modify the energy balance in the atmosphere affecting cloud development and properties (the semi-direct effect – Fan et al., (2016)). They can also serve as cloud condensation nuclei (CCN) and ice nucleating particles (INP) upon which cloud droplets and ice crystals form (the aerosol indirect effect on clouds – Rosenfeld et al., (2014)).

Advancing in aerosol knowledge faces complex challenges due to the large variability of aerosol types and in their sources and transformation processes in the atmosphere during transport. More specifically, mineral dust is the most important source of primary particles in the atmosphere with an estimated emission rate of
50   1000-3000 Tg/year representing about half of the annual particle mass emission at the global scale (Kok et al., 2021). Mineral dust sources extend over a wide area on the planet highlighting the global dust belt that extends from the arid regions of the west coast of northern Africa through the Middle East and Central Asia. Such a belt includes the Sahara Desert, which is the largest in the world being responsible for almost 50% of the global dust emissions (Kok et al., 2017). In this sense, recent studies (Kok et al., 2018) estimate
55   the direct dust-climate feedback parameter associated with the direct radiative effect in the range -0.04 to + 0.02 W/m^2°C (net, short + long wavelength), but being highly dependent on the model used. The problem with understanding the role of dust in climate becomes even more complex due to the changes in arid lands since the pre-industrial era, which is producing an increase of global dust mass loading (Kok et al., 2017). Most of these uncertainties are due to the challenges in better understanding mineral dust composition and
60   variability with size and sources (Gonçalves Ageitos et al., 2023).

Mineral dust particles are typically considered as large particles in the coarse (1-10 µm) and super-coarse (> 10 µm) modes, although recent studies have also shown the presence of a fine mode (ranges below 1 µm diameter) in mineral dust (Huang et al., 2019). The current discrepancies about the roles of fine, coarse and super-coarse modes in the dust sample (González-Flórez et al., 2023) imply difficulties in dust modelling
65   that add uncertainties to the climate modelling (Adebiyi & Kok, 2020). One critical point is the modelling of coarse mode because of the non-sphericity of these types of particles (i.e. Mishchenko et al., 2002), and also inferring the complex refractive (Formenti et al., 2003) that ultimately depends on particle size and chemical composition (González-Romero et al., 2023). For example, iron oxides are the key to understanding the mineral dust absorption properties in the UV (e.g. hematite, goethite) whilst Ca-rich
70   carbonates become important in the infrared region (Formenti et al., 2014). These variabilities in size-related and absorption parameters difficult modelling accurately response of mineral dust to direct radiative effect (Adebiyi et al., 2023). Moreover, the problem becomes even more complex because the response of dust particles interactions with other precursor gases and aerosol particles present in the atmosphere ultimately depend on dust particle composition (Ooki & Uematsu, 2005).

75   Developments in remote sensing during the last three decades have permitted global observation of dust particles worldwide. Of particular interest have been satellite observations that have allowed reaching remote areas. However, all these remote sensing observations rely on previous knowledge of aerosol phase matrix elements, which was possible thanks to laboratory measurements with polar nephelometry. Most of these laboratory studies have been made using commercial samples or specific minerals that compose dust
80   particles (Curtis et al., 2008; Huang et al., 2020; Meland et al., 2010, 2011; Muñoz et al., 2010; Volten et al., 2001), or with collected dust samples (Gómez Martín et al., 2021; J. Liu et al., 2020; Muñoz et al., 2007). Actually, the parametrizations of mineral dust phase matrix, both phase function (F_{11}) and degree of linear polarization (-F_{12}/F_{11}), used for AERONET algorithm (Dubovik et al., 2006) were calculated by fitting the laboratory measurements of different non-spherical particles samples (Volten et al., 2001).
85   AERONET parametrizations have been applied successfully worldwide and even applied to satellite retrievals of polarimetric measurements (i.e. Dubovik et al., 2011, 2019) but such parametrizations were computed from measurements at a few wavelengths, and what is more important, they might be non-representative of all ambient dust types and mixtures occurring in the atmosphere. There is therefore a current challenge in having an extended database of measurements of dust phase matrix elements for
90   different dust types and mixtures, particularly at different stages of dust evolution after their emission from the remote desert areas. These measurements would permit an advance in the understanding of mineral dust absorption properties and chemical composition (Di Biagio et al., 2017, 2019).

Thus, new measurements of aerosol phase matrix are required for ambient aerosol samples, especially in regions far from the sources and typically affected by mineral dust transport. The main challenge is in
95   optimizing polar nephelometry for continuous measurements of ambient aerosol samples. The first designs were based on using a rotating photodetector controlled by a step motor (Horvath et al., 2018) but faces with the requirement of large time to cover all angles, which is especially critical when multiwavelength polarized measurements are required. Other designs use the imaging technique to avoid these limitations but currently are limited to laboratory measurements (Moallemi et al., 2023). Synthetic tests have revealed
100   that multi-wavelength polarimetric polar nephelometry measurements improve the information content for the retrieval of aerosol optical and microphysical properties (Moallemi et al., 2022). In this sense, the

University of Maryland Baltimore County (UMBC) developed a first prototype of multi-wavelength Polarized Imaging Nephelometer (PI-Neph) capable of providing phase matrix measurements of ambient aerosol samples and took measurements during special field campaigns (Espinosa et al., 2018, 2019).
105 Recently, a commercially available PI-Neph was developed by GRASP-Earth (https://www.grasp-earth.com/) using the heritage of the developments made by UMBC. This PI-Neph was extensively tested and optimized by Bazo et al., (2024) and can provide continuous measurements of ambient aerosol phase matrix.

This work presents phase matrix measurements by the GRASP-Earth's multi-wavelength PI-Neph
110 operating in the urban background station (UGR) of the Andalusian Global ObseRvatory of the Atmosphere (AGORA). The station is located in the Southeast of the Iberian Peninsula where the main source of natural particles is the Sahara Desert's transported particles (Querol et al., 2019). We provide direct measurements of the phase matrix elements of ambient samples, which complemented by other instrumentation available at AGORA will provide unique information about mineral dust and its mixture with other particles. To that
115 end, we present the results for extreme outbreaks occurred in March 2022 (Rodríguez and López-Darias, 2024) with PM_{10} (particulate matter with diameter < 10 µm) concentrations over 1000 µgm^{-3}, and for more typical situations of moderate dust events with PM_{10} concentrations around 100 µgm^{-3}. In Section 2 we describe the experimental station and the instrumentation, Section 3 analyzes the results of the optical properties during different dust events, and Section 4 is devoted to the main conclusions and keys for future
120 work.

2   Experimental station and Instrumentation
2.1   Experimental station

Experimental measurements were carried out at the UGR station of the AGORA Observatory in the city of Granada (37.18°N, 3.58°W, 680 m asl) in Southern Spain. The main local source of aerosol particles
125 in the UGR station is road traffic (Titos et al., 2014, 2017), with sporadic presence of biomass burning aerosol (Casquero-Vera et al., 2021; Titos et al., 2017). Air-mass stagnation also favors the accumulation of pollution (Lyamani et al., 2012; Patrón et al., 2017). The city is located 200 km away from the African continent, so long-range transport of Saharan dust to the UGR station is quite common (Lyamani et al., 2010; Valenzuela et al., 2012a, 2012b). These dust intrusions have mean aerosol optical depths (AOD) of
130 0.25 ± 0.12 (Pérez-Ramírez et al., 2016) and PM_{10} concentrations ranging between 25 and 200 µgm^{-3} (Párraga et al., 2021), although extreme Saharan dust events with AOD above 1.0 also affect the station (Bazo et al., 2023; Guerrero-Rascado et al., 2009). Most of these intrusions typically occur in summer but in the last years they are becoming more frequent during the winter season (Cazorla et al., 2017; Cuevas-Agulló et al., 2024; Fernández et al., 2019; Titos et al., 2017).

135 ## 2.2   Instrumentation
2.2.1   Polarized Imaging Nephelometer (PI-Neph)

The PI-Neph (GRASP-Earth PIN-100) is used to obtain direct measurements of two aerosol phase matrix elements, the phase function (F_{11}) and the polarized phase function ($-F_{12}/F_{11}$), at three different wavelengths (405, 515 and 660 nm). Details of the instrument are in Bazo et al., (2024) and here we give a brief overview.
140 The instrument uses previous heritage in PI-Neph developments in the University of Maryland Baltimore County (Dolgos and Martins, 2014) being the novelty in the use of one beam instead of a mirror system to fold the laser beam. This feature minimizes internal reflection and loss of energy within the laser beam and guarantees that all points along the laser beam will have the same scattering plane orientation, assuring the optimal input polarization state at all scattering angles simultaneously. The optical system counts with a
145 wire grid polarizer and two liquid crystal retarders (LCVRs) that control the state of linear polarization. The light scattered by the aerosol particles is recorded with a 185° field of view CMOS camera, giving the scattered light by the particles in the sample chamber in the range 5°-175°, with 1° angular resolution. Gas calibration using well-known scatters such as particle free air and CO_2 is performed periodically, since these phase matrix elements can be computed analytically using the Rayleigh theory (Anderson et al.,
150 1996). The flow rate of the instrument is set at 10 Lmin^{-1}, and data is usually reported at 30 min or 1 hour time resolution.

The direct measurements of F_{11} and $-F_{12}/F_{11}$ allow to obtain other aerosol optical parameters such as the scattering coefficient (σ), the asymmetry parameter (g) and the fraction of backscattered light (Bs) using the following equations (Horvath et al., 2018):

$$\sigma_{sca}(\lambda) = \int_0^{180} 2\pi \frac{F_{11}(\theta,\lambda)\sin\theta}{4\pi} d\theta \,, \tag{1}$$

$$P_{11}(\theta,\lambda) = \frac{F_{11}(\theta,\lambda)}{\sigma_{sca}(\lambda)} \,, \tag{2}$$

$$g(\lambda) = \int_0^{\pi} P_{11}(\theta,\lambda) \cdot \sin\theta \cdot \cos\theta \cdot d\theta \,, \tag{3}$$

$$B_s(\lambda) = \frac{1}{2}\int_{\frac{\pi}{2}}^{\pi} P_{11}(\theta,\lambda) \cdot \sin\theta \cdot d\theta \,, \tag{4}$$

where data from 0 to 5° and from 175 to 180° have been linearly extrapolated to obtain the complete phase function (Horvath et al., 2018).

2.2.2 Additional in-situ instrumentation at AGORA

AGORA operates other in-situ instruments within the ACTRIS network (https://www.actris.eu/). The integrating nephelometer (TSI model 3563) was used to measure the aerosol particle light scattering coefficient (σ_{sca}) at 450, 550 and 700 nm with a flow rate of 15 Lmin^{-1} and a time resolution of 1 minute. As with the PI-Neph, the integrating nephelometer is calibrated with particle free air and CO_2 and Rayleigh subtraction is applied to measure particle scattering only. Due to experimental limitations the scattered light at the complete forward (0°) and backward (180°) regions cannot be detected, so the angular range for integration is 7-170°. However, results used in this work have been corrected to the entire angular range with the correction proposed by Anderson & Ogren, (1998). On the other hand, we also used the multiwavelength aethalometer (AE33, Magee Scientific) that measures aerosol light absorption coefficient (σ_{abs}) at seven different wavelengths (370, 470, 520, 590, 660, 880 and 950 nm) with a flow rate of 4 Lmin^{-1} and a time resolution of 1 minute. Equivalent black carbon (eBC) concentration is inferred by measuring the absorption coefficient at 880 nm using a mass absorption cross section of 7.77 m^{2}g^{-1} (Titos et al., 2017). Measurements of the absorption coefficient by the aethalometer are corrected with the one measured by the Multi Angle Absorption Photometer (MAAP, model 5012, Thermo Fisher) at 637 nm. More details of the instruments are in Drinovec et al., (2015) and Petzold and Schönlinner, (2004), respectively.

The scattering and absorption coefficients measured by the integrating nephelometer/PI-Neph and the aethalometer, respectively, have been used to calculate the scattering Ångström Exponent (SAE) and the absorption Ångström Exponent (AAE):

$$SAE_{\lambda_1-\lambda_2} = -\frac{\log\left(\frac{\sigma_{sca}(\lambda_1)}{\sigma_{sca}(\lambda_2)}\right)}{\log\left(\frac{\lambda_1}{\lambda_2}\right)} \,, \tag{5}$$

$$AAE_{\lambda_1-\lambda_2} = -\frac{\log\left(\frac{\sigma_{abs}(\lambda_1)}{\sigma_{abs}(\lambda_2)}\right)}{\log\left(\frac{\lambda_1}{\lambda_2}\right)} \,. \tag{6}$$

Measurements of σ_{abs} allow a direct computation of aerosol extinction coefficient ($\sigma_{ext} = \sigma_{abs} + \sigma_{sca}$) and thus obtaining more aerosol optical properties such as lidar ratio (LR) and single scattering albedo (SSA):

$$LR = \frac{\sigma_{ext}}{F_{11}(180°)} \,, \tag{7}$$

$$SSA = \frac{\sigma_{sca}}{\sigma_{ext}} \,, \tag{8}$$

where the Ångström law has been used to calculate σ_{abs} for the PI-Neph wavelengths. Note that σ_{sca} can be also obtained with the integrating nephelometer. Six months of correlative data between the TSI instrument and the PI-Neph allowed for an evaluation of the instruments, which showed excellent agreement (Bazo et al., 2024).

190 **3   Results and Discussion**
3.1 Overview of extreme dust events during March 2022

During March 2022 the Iberian Peninsula, and particularly its southeast region, was affected by two intense Saharan dust outbreaks, especially during the 15th - 16th and the 24th - 25th of March. Figure 1 shows the geopotential height maps at 850 mb for 15th March 18:00 UTC and 25th March 12:00 UTC, which are close
195 to the peaks of the event in each case. Data shown are from the NCEP/NCAR model ((Kalnay et al., 1996; Kanamitsu et al., 2002) – https://tropic.ssec.wisc.edu/archive). On 15th March, Fig. 1a indicates the low pression system centered in the southwest of the Iberian Peninsula and northern Morocco associated with low values of geopotential heights. A high-pressure system is present in the central Mediterranean associated with high values of geopotential height. This high-pressure system covers wide regions from
200 central Europe to the Sahara Desert in Libya and Tunisia. The interaction between these low-pressure and high-pressure systems favors strong southeastern winds to the south of the Iberian Peninsula. On 25th March, Fig. 1 reveals very similar patterns, although the low-pressure system is less intense (more sparse lines) and is displaced a little bit towards the east, centered over northern Morocco.
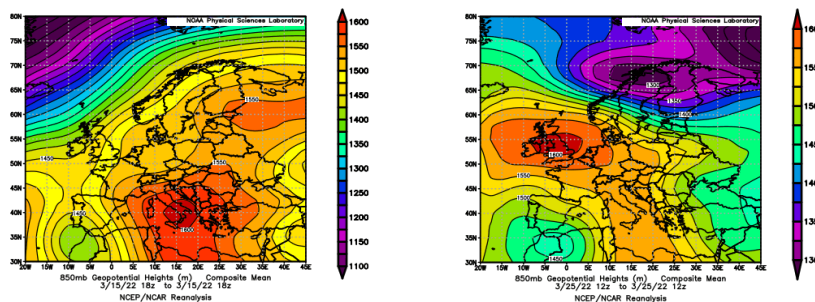
205 **Figure 1: Geopotential height at 850 mb for a) 15th March 2022 at 18:00 UTC and (b) 25th March 2022 at 12:00 UTC. Data are from NCEP/NCAR - https://tropic.ssec.wisc.edu/archive.**

The synoptic situations on the 15th and the 25th of March described in Fig. 1 implied the advection of hot and dry air from the Sahara Desert region in Argelia and southern Morocco. The low-pressure system favored wind gusts and thus the injection of dust particles in the atmosphere, which are later transported
210 long distances by the low-pressure system. This is one of the classical transport patterns of Saharan dust to the Iberian Peninsula (Escudero et al., 2005; Rodríguez et al., 2001; Salvador et al., 2014). Figures 2 and 3 show total aerosol optical depth (AOD) at 550 nm generated by the CAMS model (Benedetti et al., 2009; Morcrette et al., 2009) over Europe. The wind field at the surface is also represented in these Figs. Figure 2 clearly shows the counterclockwise winds associated with the low-pressure system and how this hot and
215 dry air enters through the southeast reaching the north of the Iberian Peninsula and southern France. That airmass also transports large amounts of mineral dust particles as can be observed by the high values of simulated AODs. It is observed that the largest intensity of dust particles in the southeast of the Iberian Peninsula happened on the evening of 15th March. For the 25th of March, the wind pattern is very similar to that on 15th March, although it does not reach the same northern locations. Indeed, the low-level system
220 configuration seems to facilitate the transport of this hot and dry air to western locations in Portugal and the Atlantic Ocean. The CAMs model also predicts a larger amount of dust particles as indicated by the high AODs.
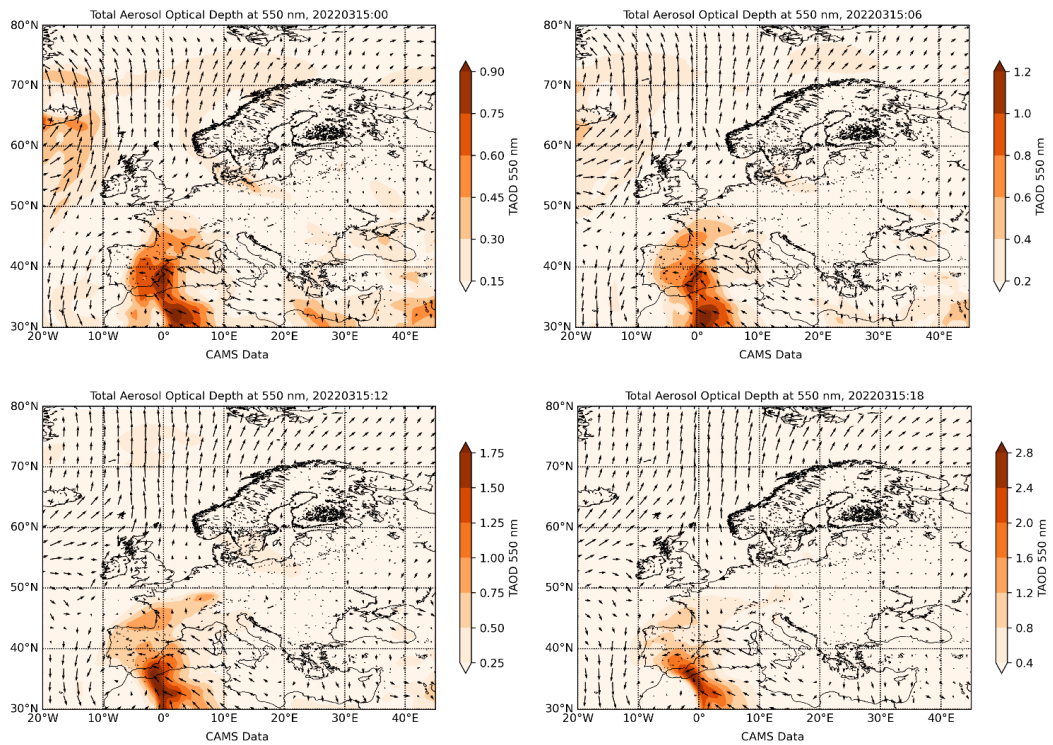
Figure 2: CAMS model simulations of total aerosol optical depth (TAOD) and wind field for different times on 15th March 2022.
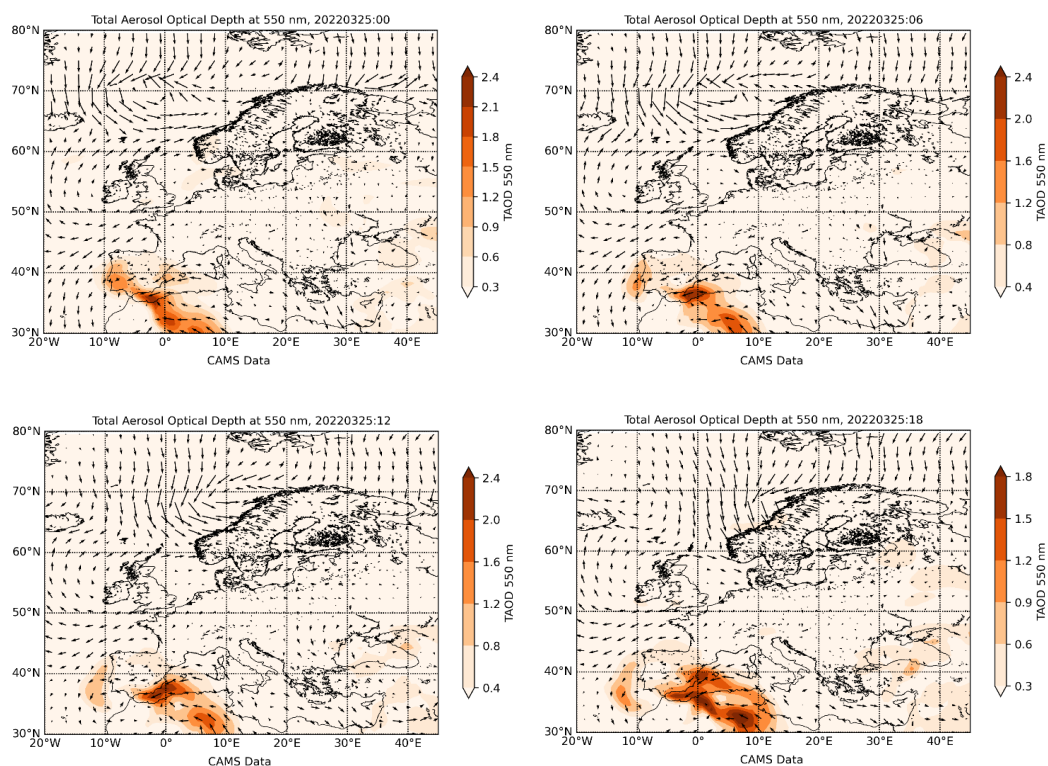
Figure 3: CAMS model simulations of total aerosol optical depth (TAOD) and wind field for different times on 25th March 2022.

Figure 4 shows satellite images provided by NASA worldview (https://wvs.earthdata.nasa.gov) that allow to have a visualization of the intensity of the dust outbreaks over the Iberian Peninsula. On both days, there was presence of clouds in the Iberian Peninsula because of the advection of humidity from the Atlantic by the low-pressure system, more intense on 25th which explains that almost all the Iberian Peninsula was covered by clouds. The image for 15th March clearly shows high presence of dust in the north of the Iberian Peninsula, the Cantabrian Sea and southern France. For the 25th of March the cloud cover hinders dust visualization, but it is observed in the Atlantic in the region between the Canary and Madeira islands. We highlight that such extreme events are not typical in winter season in the Iberian Peninsula, although it is not the first time that similar dust events have been registered in this season (Cazorla et al., 2017; Fernandez et al., 2019; Titos et al., 2017).

The events on 15th and 25th March 2022 can be considered as extreme Saharan dust outbreaks because of the large area covered, but especially because of the large amount of mineral dust particles transported. A more in-depth analysis of satellite images revealed that for the cloud-free pixel registered AODs were between 1.9 - 2.5 on 15th March and between 0.3 – 1.5 on 25th March, which are very high for these locations (Pérez-Ramírez et al., 2012). The extremely high AODs values on 15th March associated with dust particles were confirmed by AERONET observations with AODs above 1.0 for the stations in northern Spain (A Coruña and Palencia) and southern France (Aubiere, Agen, Archaon and Momuy) where data of Level 2.0 Version 3 are available – graphs not shown for clarity but can be visualized in AERONET webpage (https://aeronet.gsfc.nasa.gov/). Unfortunately, there is no AERONET data Level 2.0 Version 3.0 available on 25th March due to cloud-coverage in the AERONET stations. For both events, the urban background air-quality surface station in Granada (Palacio de Congresos (PAL)) http://juntadeandalucia.es/medioambiente) registered 10-minute PM$_{10}$ concentrations, being up to 2500 µgm^{-3} on the 15th of March and up to 800 µgm^{-3} on the 25th of March, values that are way above the usual PM$_{10}$ values registered at Granada during usual dust outbreaks (Párraga et al., 2021).
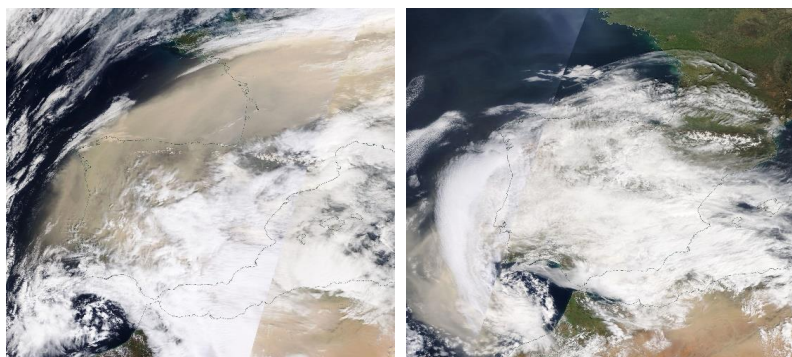
Figure 4. (a) Satellite image from 15ᵗʰ March 2022. (b) Satellite image from 25ᵗʰ March 2022. (Images from https://wvs.earthdata.nasa.gov).

3.2 Aerosol phase matrix from different dust scenarios
3.2.1 Extreme events
3.2.1.1 General overview

For the two extreme events registered on 15ᵗʰ and 25ᵗʰ March 2022, Fig. 5 shows hourly averages of different aerosol properties obtained by the in-situ instruments at UGR station. In particular, we show eBC concentrations measured by the AE33, $\sigma_{sca}(\lambda)$ measured by the PI-Neph, and SAE, AAE (both calculated between 405 and 660 nm), $g(\lambda)$, $Bs(\lambda)$, $SSA(\lambda)$ and $LR(\lambda)$ derived from measurements of both instruments. PM_{10} concentrations are also shown, which were obtained from the PAL air-quality station (~ 600 m distance from UGR station). Panel (a) in Fig. 5 shows the results for the event on 15ᵗʰ - 16ᵗʰ March, where the lack of data in the AAE, SSA and LR time series (Fig. 5a.6) is due to the absence of AE33 data during this event, while Panel (b) shows data for the event on 24ᵗʰ - 25ᵗʰ March.

For the event on 15ᵗʰ - 16ᵗʰ March, Fig. 5a.1 reveals extremely high PM_{10}, with an average of 794 μgm^{-3} for the period shown, being over the daily limit value of 50 μgm^{-3} (2008/50/CE European Directive). Maximum values of hourly PM_{10} concentrations are registered at around 16 UTC, with values reaching almost 1800 μgm^{-3}. The scattering coefficient time series shows the same behavior as the PM_{10}, with maximum values of σ_{sca} at the same time as the peak of the PM_{10} concentration. The mean value (±std) of SAE is 0.01 ± 0.15, which increases to 0.20 when PM_{10} concentrations reach their maximum. Such values of SAE suggest clear predominance of large particles. The time series of g during 15ᵗʰ March (Fig. 5a.4) shows approximately constant values, with mean values of 0.672 ± 0.010, 0.701 ± 0.006 and 0.729 ± 0.007 for 405, 515 and 660 nm, respectively, which are typical values for transported dust particles (Horvath et al., 2018). Also, Horvath et al. (2018) found an averaged Bs of 0.094 at 532 nm for Saharan dust, which agrees with the results shown in Fig. 5a.5 for the 515 nm wavelength (0.098 ± 0.003). Low values of the Bs at the three wavelengths are related to small values of F_{11} at the backward scattering angles, which is common for non-spherical particles. The lack of aethalometer data did not allow eBC, AAE, SSA and LR analyses for this day.
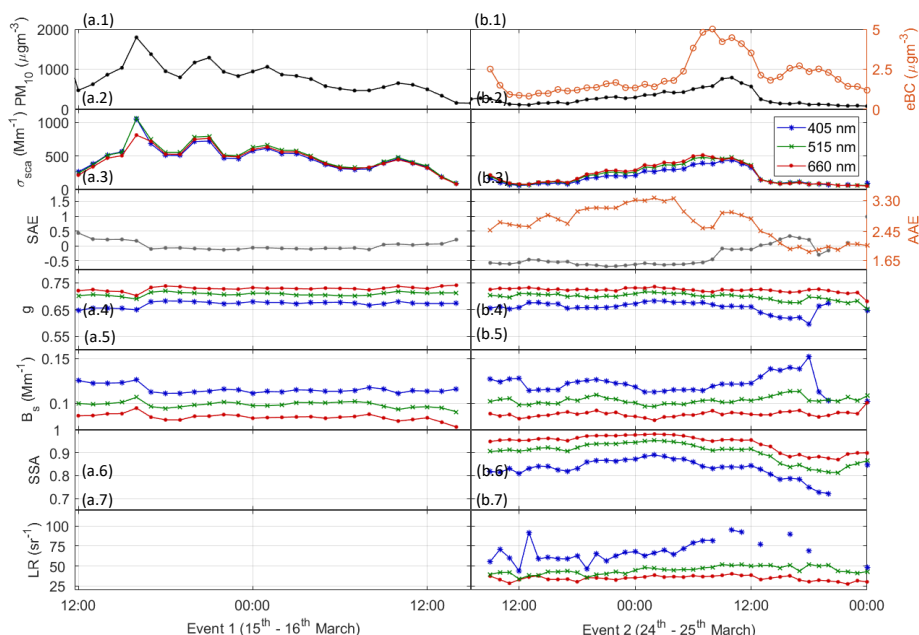
Figure 5. Time series of the PM$_{10}$ and EBC concentrations (a.1, b.1), σ$_{sca}$ – scattering coefficient (a.2, b.2), SAE – scattering Angström exponent and AAE – absorption Angström exponent (a.3, b.3), g – asymmetry parameter (a.4, b.4), Bs – fraction of backscattered light (a.5, b.5), SSA – single scattering albedo (a.6, b.6) and LR – lidar ratio (a.7, b.7) for the extreme dust events of 15th March (a) and 24th March 2022 (b).

For the dust event on 24th - 25th March, the average PM$_{10}$ concentration is 283 µgm^{-3}. These PM$_{10}$ concentrations (Fig. 5b.1) increase until 10 UTC, when reach the maximum hourly value of 790 µgm^{-3}. These values are lower than those registered on 15th March, but again they are very high and above the daily limit of the European Directive. Scattering coefficients in coincidence with the PM$_{10}$ concentration peak are 468, 476 and 441 Mm^{-1} for the 660, 515 and 405 nm wavelengths, respectively. After this peak, both PM$_{10}$ and σ$_{sca}$ decrease, suggesting the end of the dust event over the station. The SAE main feature is its approximately constant value of –0.5 until early in the morning on 25th March when it slightly starts to increase. This pattern suggests clear predominance of large particles during this stage of the dust outbreak, while the increase in the morning can be associated with additional influence of small particles, likely originated from road traffic during morning traffic rush hours. On the other hand, the AAE shows a different behavior, with high values at the beginning of the time series representative of mineral dust and a later decrease to values around 1.7 coincident with the decrease in PM$_{10}$. These values of AAE are in the range of those reported by Valenzuela et al., (2015) for usual dusty conditions, where there is mixture of dust and black carbon particles. This agrees with the patterns of eBC and PM$_{10}$, suggesting a larger contribution of eBC to the total PM$_{10}$ concentration at the end of the dust event than at the peak. On the other hand, g mean values are 0.659 ± 0.020, 0.698 ± 0.013 and 0.723 ± 0.009 for 405, 515 and 660 nm, respectively. The Bs (Fig.5.5) shows a similar behavior than in the previous event (Fig. 5a.5), with values around 0.1 for the 515 nm wavelength and below 0.15 in the three channels. The channel at 405 nm seems to be the most sensitive in g and Bs to changes in dust concentration since the time when a sharp change happens (25th March at 14:00 UTC) coincides with the hour when PM$_{10}$ decreases and eBC increases indicating more contribution of eBC to the total ensemble of particles. Aethalometer measurements on that day allowed to study further optical properties: the SSA (Fig. 5b.6) shows high values for all three wavelengths at the beginning of the event, that is, when the dust concentration was higher. However, there is a strong spectral dependency, since the SSA at 405 nm clearly shows lower values (~0.85) compared to the other wavelengths, that present SSA above 0.9. As the PM$_{10}$ concentration decreases (and eBC concentration increases), the SSA shows smaller values, with a stronger decrease in the 405 nm wavelength. Lastly, Fig. 5b.7 shows the time series

of the LR during the second dust event, on 15th March. The LRs at 515 nm and 660 nm are rather constant, with mean values of 45 ± 5 sr^{-1} and 35 ± 3 sr^{-1}, respectively. However, the LR at 405 nm shows higher

320 values and variability, with 67 ± 15 sr^{-1}. LR at 515 nm is very similar to those measured by lidar systems at 532 nm for transported Saharan dust layers (Groß et al., 2013). Thus, the hypothesis that after 14:00 the presence of pollution particles becomes more relevant implies a decrease in SSA and variability in LRs, particularly in 405 nm.

3.2.1.2 Phase matrix characterization

325 Figure 6 shows F_{11} and $-F_{12}/F_{11}$ phase matrix elements for the event on 15th - 16th March 2022 at four different representative stages. Data are 60-minutes averages. Detailed hourly evolutions can be found in the Supplementary Material (Figs. S1-S2). Mean hourly averages for the time periods shown in Fig. 6 are given in Table 1, particularly PM_{10}, eBC, σ_{sca}, SAE, AAE and g – note that SSA and LR were not available due to the lack of Aethalometer data for that day. Figure 6a represents the phase matrix elements on 15th

330 March 07:00 UTC before the Saharan dust outbreak reached the station and represents background conditions. Figure 6b (15th March 12:00 UTC) illustrates the strong influence of mineral dust, whereas Fig. 6c (15th March 17:00 UTC) corresponds to the peak of the intrusion with the largest PM_{10} concentrations. Finally, Fig. 6d (16th March 13:00 UTC) shows the matrix elements after the maximum concentrations when dust begins to decrease.

335 Figure 6 shows a general pattern in F_{11} characterized by strong predominance of forward scattering up to two orders of magnitude greater than backward scattering. However, there are significant changes in both magnitude and spectral dependence over time, that is, with the intensity of the dust outbreak passage. At the beginning of the dust event (Fig. 6a), the values of F_{11} in the forward scattering region are around 1000 Mm^{-1}sr^{-1} for all three wavelengths. The F_{11} matrix element shows a slight increase in the backward region

340 and there is notable spectral separation. Table 1 data suggest the presence of fine mode particles with SAE of 1.65 ± 0.13 and g and Bs parameter suggesting presence of spherical particles. However, as higher concentrations of mineral dust reached the UGR station, resulting in higher PM_{10} levels and strong reduction in SAE (Table 3), F_{11} began to show greater values in the forward scattering region, being around 10000 Mm^{-1}sr^{-1} for the three channels of the PI-Neph with almost no spectral differences. There are still

345 some spectral differences in the backward scattering angles, but the behavior of the F_{11} in that area becomes more constant than in the previous case (Fig. 6a). At the peak phase of the event (Fig. 6c), values of F_{11} in the forward scattering region reach around 50000 Mm^{-1}sr^{-1} for the three channels, while the backward region shows a constant tendency. Also, there is no spectral separation among different wavelengths. Figure 6d shows the scattering matrix elements at an advanced stage of the dust event. The contribution of large

350 particles is still important, given the large values of $F_{11} \sim 10000$ Mm^{-1}sr^{-1} in the forward scattering region. However, there are some spectral differences in the middle and the end of the angular range.

The study of $-F_{12}/F_{11}$ indicates significant differences at the different stages of the dust outbreak. At the beginning $-F_{12}/F_{11}$ shows very different spectral patterns with remarkable spectral separation: for 515 and 660 nm, $-F_{12}/F_{11}$ follows bell-shaped patterns with values near to zero at the edges (0° and 180°) and a

355 maximum around 90° of 0.4 and 0.5 for 515 and 660 nm respectively. However, for 405 nm, the pattern is markedly different, with maximum values of 0.1 occurring at around 80°, followed by a sharp decrease, reaching negative values of -0.4 close to 150°. For the two following cases (Figs. 6b.2 and 6c.2), which correspond to higher PM_{10} concentration values, $-F_{12}/F_{11}$ shows a distinct pattern. This pattern is characterized by almost negligible differences with wavelength and a very small bell-shaped pattern with

360 maxima around 0.1 at 90° (Volten et al., 2001). Later, after the strong dust passage, Fig. 6d.2 shows a similar bell-shape pattern at 515 and 660 nm, but there is presence of some negative values at 405 nm. The differences in $-F_{12}/F_{11}$ patterns and wavelengths dependences with time can serve to differentiate different particle types in the ensemble of particles measured and will be studied further in this section.
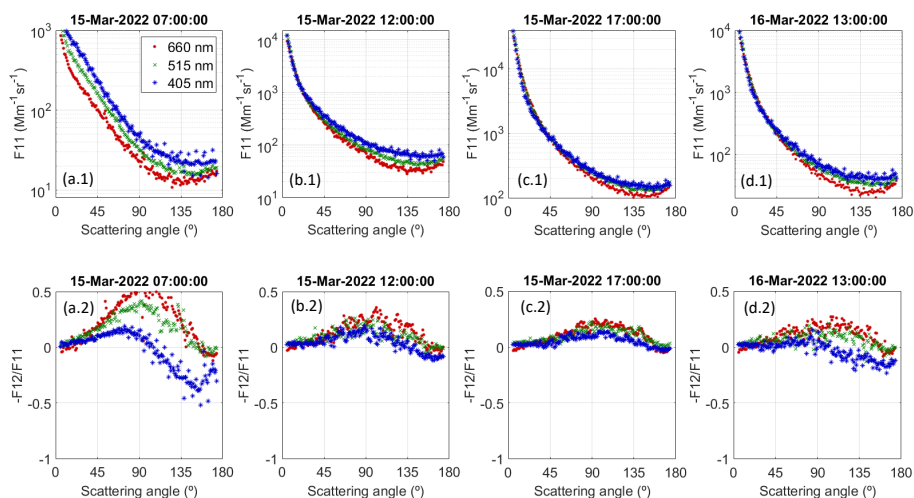
Figure 6. Phase function (F_{11}) and polarized phase function ($-F_{12}/F_{11}$) for four different moments of the evolution of the dust event on 15th - 16th March 2022,

Similarly, for the event on 24th - 25th March Fig. 7 shows F_{11} and $-F_{12}/F_{11}$ phase matrix elements for four different representative moments during the event. The data correspond again to 60-minute averages, with detailed hourly evolutions shown in the Supplementary Material (Figs. S3-S4). Mean hourly averages for these periods of PM_{10}, EBC, σ_{sca}, SAE, AAE g, SSA and LR are also in Table 1. Once again, this event exhibits lower values in particulate matter and appears to be less intense when compared to the event on 15th -16th March. However, it can still be considered an extreme event because the maximum PM_{10} concentrations registered are above the typical values registered in the UGR station (Párraga et al., 2021). The temporal evolution selection serves to follow the conditions before the arrival of the dust outbreak (24th March 13:00 UTC), the entrance of the strong Saharan dust (24th March 21:00 UTC) and the conditions during the outbreak peak (25th March 09:00 UTC), with the final conditions after the dust outbreak (25th March 20:00 UTC).

Figure 7 shows that F_{11} patterns are very similar to the previous extraordinary event on 15th - 16th March, with strong predominance of forward scattering (~25000 $Mm^{-1}sr^{-1}$) being two orders of magnitude above the backscattering (~100 $Mm^{-1}sr^{-1}$) at the peak of the event on 25th March 9:00 UTC, with minimum spectral dependency. Nevertheless, there are some changes in F_{11} with the different situations: the decrease in F_{11} in the forward scattering region becomes sharper when the PM_{10} concentrations are higher (Figs. 7b.1 and 7c.1), which could be explained by the presence of irregular dust particles (Volten et al., 2001). For the backward region F_{11} shows a flatter behavior for high PM_{10} concentrations (Figs. 7b.1 and 7c.1), while for the cases with lower PM_{10} concentrations there is a sharp increase in scattering from 150° to 180°. During the previous extreme dust outbreak, we observed flat patterns for the backward scattering region during the peaks of the dust intrusions. There are no spectral dependences, which could suggest that these are the patterns when there is a large predominance of dust in the atmosphere, as observed in the laboratory (Muñoz et al., 2007; Volten et al., 2001).

390
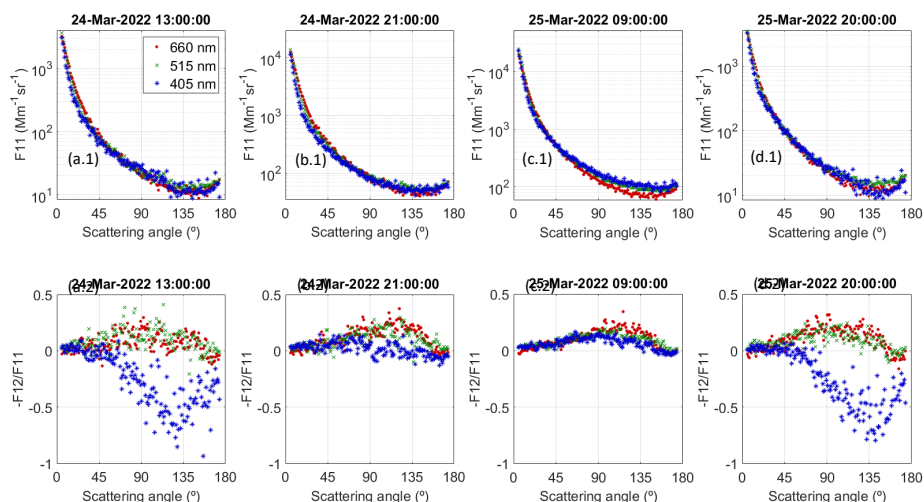
Figure 7. Phase function (F_{11}) and polarized phase function (-F_{12}/F_{11}) for three different moments of the evolution of the dust event on 24th - 25th March 2022.

In contrast to F_{11}, -F_{12}/F_{11} exhibits again several behaviors throughout the event, providing greater insight

395 into the sampled aerosol. During the peak of the event on 15th-16th March, the of -F_{12}/F_{11} patterns show minimal differences with wavelength and a very small bell-shaped pattern with maximums around 0.1 at 100°. This pattern is clearer on 25th March at 09:00:00 UTC that corresponds with the peak of the dust intrusions, while on 24th March 21:00 UTC (a few hours before the maximum PM$_{10}$) it is observed a drift of the maximum in the bell to lower scattering angles with shorter wavelengths. However, the big

400 differences are observed for the moments before the arrival of the dust outbreak on 24th March 13:00 UTC and when the dust is withdrawing on 25th March 20:00 UTC. In these two cases -F_{12}/F_{11} shows bell-shape patterns for 515 and 660 nm, with maximums of approximately 0.2 around 100° and values close to zero in the regions for scattering angles below 50° and above 150°. These patterns agree with the observed for the other moments of the intrusion and with those of the previous event on 15th-16th March. However, the

405 pattern for 405 nm is markedly different from the rest, as observed in the event on 15th-16th March. It is characterized by almost flat values close to zero of -F_{12}/F_{11} in the range of approximately 0° - 50°, followed by a sharp decrease reaching negative values of -0.6 close to 130°. Then, there is a sharp increase in -F_{12}/F_{11} reaching values close to zero at 180°. Therefore, -F_{12}/F_{11} at 405 nm appears to be highly sensitive to the possible influence of other particles in the mixture. It is also noteworthy that the maximum in eBC coincides

410 with the maximum of PM$_{10}$, but the contribution of eBC to the total aerosol burden is lower due to the high concentrations of dust. This can explain the dust-like pattern of -F_{12}/F_{11} at the peak of the event.

Table 1. Hourly averaged properties of different moments of the extreme dust outbreaks in March 2022 reported in Figs. 6 and 7. The properties are reported at three wavelengths in the order of 660, 515 and 405 nm from top to bottom. The angular range of the PI-Neph is used as the integration range of σ_{sca}.

	PM$_{10}$ (µgm^{-3})	eBC (µgm^{-3})	σ_{sca} (Mm^{-1})	SAE	AAE	g	Bs (Mm^{-1})	SSA	LR (sr^{-1})
15th Mar 07:00	61 ± 5	-	55 ± 3	1.65 ± 0.13	-	0.573 ± 0.015	0.135 ± 0.013	-	-
			84 ± 4			0.604 ± 0.018	0.117 ± 0.011		
			123 ± 7			0.616 ± 0.008	0.116 ± 0.004		
15th Mar 12:00	473 ± 131	-	215 ± 36		-	0.722 ± 0.001	0.086 ± 0.005	-	-

Date/Time	PM10	eBC	σsca	SAE	AAE	g	Bs	SSA	LR
			241 ± 38	0.43 ± 0.13		0.703 ± 0.001	0.100 ± 0.007		
			265 ± 39			0.641 ± 0.001	0.126 ± 0.005		
15th Mar 17:00	1376 ± 256	-	718 ± 128	-0.11 ± 0.12	-	0.734 ± 0.008	0.084 ± 0.005	-	-
			746 ± 112			0.715 ± 0.009	0.096 ± 0.005		
			682 ± 101			0.679 ± 0.009	0.113 ± 0.006		
16th Mar 13:00	338 ± 48	-	178 ± 47	0.07 ± 0.13	-	0.739 ± 0.008	0.079 ± 0.005	-	-
			191 ± 52			0.713 ± 0.008	0.095 ± 0.005		
			184 ± 50			0.673 ± 0.011	0.113 ± 0.006		
24th Mar 13:00	108 ± 14	0.81 ± 0.10	76 ± 13	-0.46 ± 0.22	2.58 ± 0.10	0.733 ± 0.024	0.084 ± 0.014	0.955 ± 0.004	36 ± 10
			70 ± 12			0.709 ± 0.031	0.098 ± 0.020	0.912 ± 0.006	38 ± 11
			65 ± 8			0.664 ± 0.035	0.117 ± 0.018	0.832 ± 0.006	92
24th Mar 21:00	297 ± 21	1.59 ± 0.14	284 ± 27	-0.69 ± 0.18	3.09 ± 0.03	0.725 ± 0.025	0.088 ± 0.016	0.975 ± 0.001	34 ± 4
			257 ± 25			0.701 ± 0.025	0.105 ± 0.017	0.940 ± 0.001	40 ± 6
			205 ± 16			0.659 ± 0.021	0.124 ± 0.015	0.867 ± 0.003	57 ± 7
25th Mar 09:00	760 ± 44	4.21 ± 0.21	466 ± 15	-0.09 ± 0.06	2.96 ± 0.05	0.725 ± 0.007	0.087 ± 0.005	0.957 ± 0.002	39 ± 5
			461 ± 17			0.705 ± 0.009	0.101 ± 0.006	0.915 ± 0.003	52 ± 6
			427 ± 14			0.662 ± 0.007	0.122 ± 0.005	0.838 ± 0.005	-
25th Mar 20:00	116 ± 6	2.3 ± 0.5	80 ± 7	-0.16 ± 0.18	2.03 ± 0.08	0.722 ± 0.019	0.086 ± 0.011	0.876 ± 0.015	32 ± 7
			78 ± 6			0.689 ± 0.020	0.104 ± 0.014	0.815 ± 0.020	52 ± 18
			74 ± 3			0.667 ± 0.021	0.113 ± 0.011	0.722 ± 0.021	-

3.2.2 Moderate dust events during spring/summer 2022

The PI-Neph also continuously operated from April to September 2022 and other events of Saharan dust transport were registered at the UGR station. However, these outbreaks did not exhibit such an extreme dust transport when compared with the events on March 2022. Actually, hourly averaged PM10 levels were below 130 μgm^{-3} and σsca below 130 Mm^{-1}, which are typical values observed at the UGR station during Saharan dust outbreaks (Lyamani et al., 2010). For this entire period of measurements (Apr 14th to Sep 9th) Fig. 8 shows hourly averages of PM10 and eBC concentrations, σsca(λ), SAE, AAE (both calculated in the 405-660 nm range), g, Bs, SSA and LR. For easy identification of dust influence conditions, data shown in Fig. 8 are filtered out and correspond only to values of SAE< 1, which are used as a proxy for the presence of dust particles in the atmosphere (Lyamani et al., 2010). Moreover, some studies suggest that the variability in SAE can serve as an indicator of the different mineral dust mixtures with urban background pollution (Teri et al., 2024).

The period with the least frequency of dust events is April - June, although the few cases detected show high values of PM10 concentrations and the scattering coefficients with SAE values closer to 1, suggesting high degree of mixture between dust and pollution. Also, this period presents large spectral dependency in g and Bs, with g ranging between 0.5 and 0.7, and Bs ranging from 0.13-0.18, which are typical values

more related to non-Saharan dust aerosols (Horvath et al., 2018). Moreover, SSA shows large variability ranging from 0.5 to around 0.9 for all three wavelengths, where the lower limit of the range suggests the presence of absorbing particles in the sample. This is also supported by the AAE with values close to 1, typical of BC.

435 During the summer season there is more frequency of Saharan dust intrusions, which is typical in the UGR station (Perez-Ramirez et al., 2016). Generally, there is more variability in all parameters, suggesting more complex mixtures of dust with other particles: the asymmetry parameter, which is wavelength dependent, shows very similar values to those obtained during spring, but with important variability ranging between 0.55 and 0.75. SAE and AAE show values between 0 and 1 and between 1 and 2, respectively, which are

440 the typical values when there is influence of dust particles in our station (Valenzuela et al., 2015). The outliers in the summer season with negative SAE close to –0.5 and AAE of up to 2.5 might be associated with cases that have more presence of dust. In summer season the largest values of AAE (close to 2) are observed when compared with the spring season, which can be interpreted as fewer absorbing particles. SSA shows very similar values to those obtained during the spring season.

445 The LR is a critical variable for lidar systems and it strongly depends on $F_{11}(180°)$ and absorption, which makes it very sensitive to the different mixtures of particles in the atmosphere. Thus, results of Fig. 8 serve to illustrate LR variability for dusty conditions but with influence of other types of particles. Generally, Fig. 8 shows values between ~40 sr^{-1} and 100 sr^{-1} for the three wavelengths. The lower limits are closer to the values for pure dust while the upper values are typical values registered for predominance of

450 anthropogenic particles (Müller et al., 2007). Thus, results of Fig. 8 indicate the large sensitivity of LR to changes in the mixture of particles. Particularly, the values in spring – although there is less data – are above 75 sr^{-1} with little spectral dependence, suggesting that the presence of fine particles in the mixture are ultimately responsible for LR values. During the summer seasons the lower values around 40-50 sr^{-1} are more frequently registered with larger spectral variabilities, suggesting that now LR values are

455 determined by the predominance of coarse particles.

To gain better understanding of the evolution of the phase matrix elements in different cases of dust mixtures with anthropogenic particles, Fig. 9 shows the phase matrix elements for three different dust events represented by the black boxes in Fig. 8. Particularly, Fig. 9 shows hourly averages of F_{11} and -F_{12}/F_{11} for these three selected events. Table 2 summarizes hourly mean values of PM$_{10}$ and spectral σ_{sca},

460 g, Bs, LR and SSA, plus mean values of SAE and AAE for these selected cases. Table 2 results show an insight into these three cases. The first event on 16th April is the one with largest contribution of urban background pollution to the mixture. The flat spectral pattern in SSA might suggest that absorption is mostly explained by black carbon particles because mineral dust usually presents a spectral pattern with lowest SSA in the UV (Dubovik et al., 2002). The values of g suggest the higher predominance of spherical

465 particles when compared to the other cases, so it is likely that the urban background particles suffered aging processes, leading to more spherical shapes (Leskinen et al., 2023). For the case on 5th July, mineral dust particles are more relevant. Nevertheless, the more pronounced spectral SSA when compared to 16th April also relates to the influence of dust in absorption (Dubovik et al., 2002). Finally, the case on 30th August is the one with the largest PM$_{10}$ concentrations but also with the largest eBC, which can make a very complex

470 mixture.
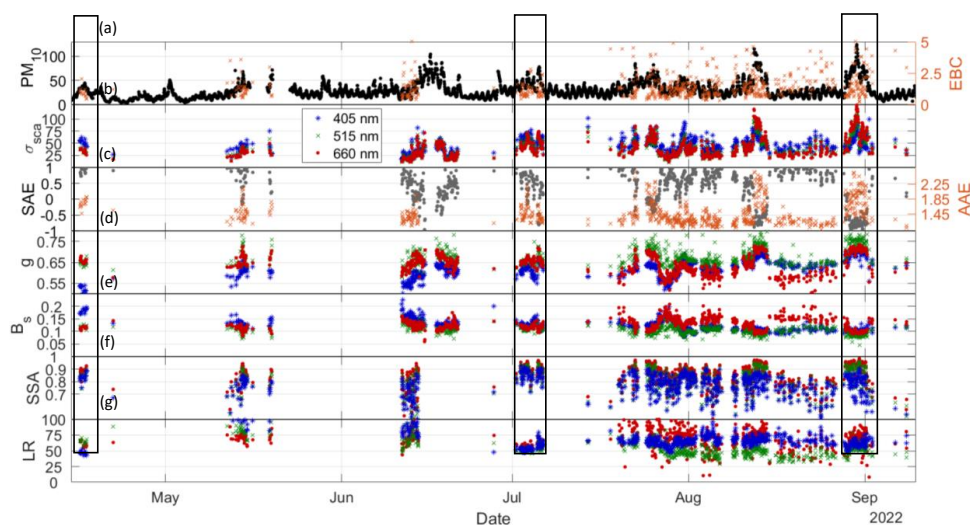
Figure 8. Time series for the moderate dust events of 2022 of the PM₁₀ and EBC concentrations (μgm⁻³) (a), σ_sca – scattering coefficient (Mm⁻¹) (b), SAE – scattering Angström exponent and AAE – absorption Angström exponent (c), g – asymmetry parameter (d), Bs – fraction of backscattered light (Mm⁻¹) (e), SSA – single scattering albedo (f) and LR – lidar ratio (sr⁻¹) (g). All optical properties are shown at 405, 515 and 660 nm. Black boxes represent three different events on 16th April, 5th July and 30th August 2022.

Table 2. Hourly averaged properties of different dust events in 2022. For properties reported at three wavelengths, the order is 660, 515 and 405 nm (top to bottom). The integration range of σ_sca is the angular range of the PI-Neph.

	PM₁₀ (μgm⁻³)	eBC (μgm⁻³)	σ_sca (Mm⁻¹)	SAE	AAE	g	Bs (Mm⁻¹)	SSA	LR (sr⁻¹)
16th Apr	36	0.92	31	0.94	1.71	0.641	0.119	0.878	59
			31			0.630	0.126	0.837	61
			48			0.505	0.193	0.830	43
5th Jul	76	1.07	61	-0.46	1.37	0.712	0.097	0.930	61
			53			0.694	0.109	0.892	58
			49			0.656	0.114	0.843	66
30th Aug	124	2.42	129	-0.86	1.73	0.711	0.096	0.920	67
			115			0.761	0.080	0.882	58
			85			0.701	0.104	0.789	63

Figure 9 shows that all F₁₁ cases exhibit the typical pattern for large and non-spherical particles characterized by large predominance of scattering in the forward region, although there is no flat behavior of the curve in the backward scattering characteristic of this type of particles (Muñoz et al., 2007). The region between 140°-160° exhibits minimum values with a subsequent increase, suggesting the presence of some spherical particles in the sample. However, there are differences between the events shown. In the case of the first dust event on 16th April (Fig. 9a), a strong spectral dependency is observed between 405 nm and the other wavelengths from 30° on, which is not observed for the other events. The largest contribution of urban pollution to the mixture can be one of the reasons for these spectral variations on 16th April. Another possible reason could be the less influence of absorbing particles as this case also presents the lower eBC and largest SSA when compared with the other two cases. The cases with almost negligible spectral differences could be explained by a more predominance of big particles. Thus, the discussion of these three selected cases illustrates that even though dust predominant cases present a classical scattering pattern characterized by strong forward scattering, the spectral dependences and the shape of the forward scattering depends ultimately on the mixture of particles.

495
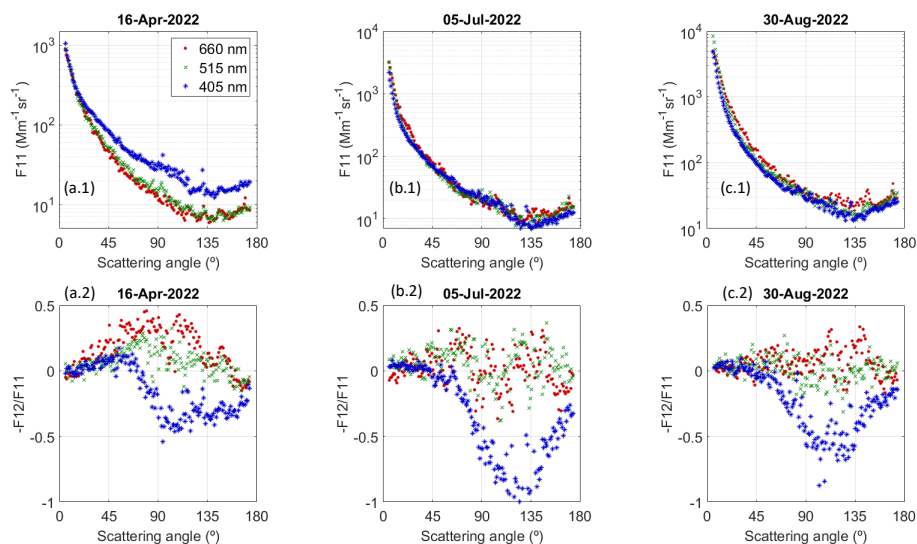
Figure 9. Phase function (F_{11}) (1) and polarized phase function (-F_{12}/F_{11}) (2) for different moderate dust events: (a) 15th April 2022 (b) 5th July 2022 and (c) 30th August 2022.

Figure 9 shows that -F_{12}/F_{11} presents very similar patterns for the three cases. The patterns are characterized
500 by a bell-shape for the 515 and 660 nm channels with maximums in the region around 100°, with noise in the two summer events. However, the -F_{12}/F_{11} pattern in 405 nm shows a very different behavior, having positive -F_{12}/F_{11} values until ~ 70° and negative -F_{12}/F_{11} values for the following angles. Minimum -F_{12}/F_{11} values are in the region around 120°. The noisy values in 660 and 515 nm suggest the complexity of the ensemble of particles measured, and thus these channels seem to be very sensitive to the aerosol mixtures.
505 On the other hand, the pattern at 405 nm is clearly different, so the -F_{12}/F_{11} at this wavelength could be a potential proxy for studying the mixture of particles in the sample. It is noted that the patterns observed for F_{11} and for -F_{12}/F_{11} are similar to those observed during the extreme events on 15th – 16th March and 25th – 26th March, when dust entered and withdrew. The pattern observed in -F_{12}/F_{11} for 405 nm was also observed in cases with influence of pollution at the UGR station in Bazo et al. (2024). Therefore, polarization
510 measurements seem to be ideal for studying the different types of mixtures of dust particles with others of anthropogenic origin.

3.2.3 Comprehensive assessment of the different dust events

To gain more insight about aerosol mixtures during the extreme dust event on 24th – 25th March 2022 and the rest of dust cases registered in the period April – September 2022 we use the typing methodology
515 defined in Cazorla et al., (2013) and modified in Schmeisser et al., (2017), based on optical properties. To that end, Fig. 10 shows SAE versus AAE, being both parameters computed in the range 450 -700 nm. The different types of aerosol are also illustrated depending on AAE and SSA values using the methodology proposed by Schmeisser et al., (2017). Different colors are used to identify different stages in the temporal evolution for the extreme dust event on 24th – 25th March. Note that for the event on 15th - 16th March there
520 were no aethalometer data and thus no measurements of AAE.
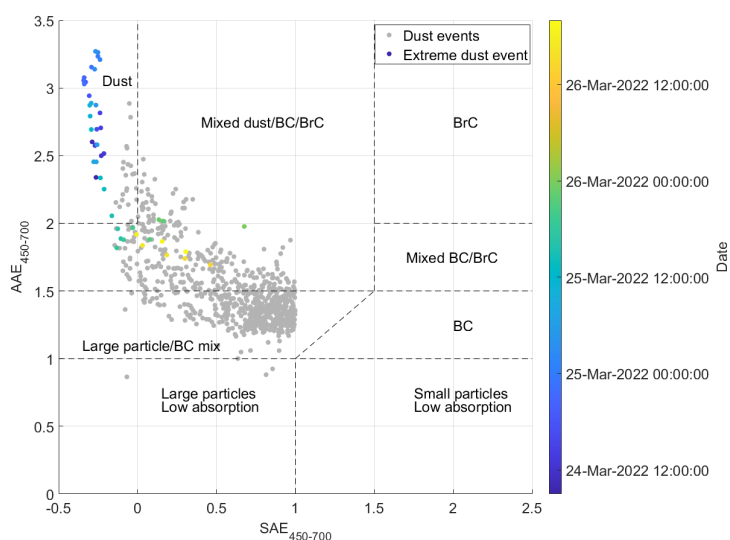
Figure 10. Absorption Angström exponent (AAE) versus scattering Angström exponent (SAE) for the extreme dust event on 24th - 25th March 2022 (colored markers) and for the moderate dust events registered in the UGR station during the period April-September 2022 (gray markers). Both intensive properties have been calculated in the range 450-700 nm. Colorbar indicates the temporal evolution of the extreme dust event on 24th - 25th March. Classification of different aerosol types following the method proposed by Schmeisser et al., (2017) is also shown.

Figure 10 shows that for the data points of the extreme dust outbreak on 24th- 25th March 2022 most of the data fall into the region of pure dust type, particularly those registered at beginning of the dust event when the PM$_{10}$ concentrations were extremely high and the large predominance of mineral dust in the sample is evident. As the dust event evolves, particularly from 26th March 2022, the data points start to fall in the region mixed dust/BC/BrC. This coincides with the drop of PM$_{10}$ concentration and increase of eBC observed in Fig. 5. Therefore, there could be a more balanced contribution of both urban background pollution and mineral dust to the ensemble of particles in the sampled air. If we compare these typing features with the scattering matrix elements on 24-25th March 2022 (Fig. 7), we observed that for the cases typed as pure dust the -F$_{12}$/F$_{11}$ follows a bell-shape pattern for all wavelengths. However, for the cases classified as mixtures, there was a different pattern -F$_{12}$/F$_{11}$ for the 405 nm channel. Thus, the typing classification explains the differences in the phase matrix for the temporal evolution of the extreme dust event 24th-25th March 2022. This is particularly critical for -F$_{12}$/F$_{11}$ and we can then conclude that polarization measurements are ideal to identify differences in aerosol types that initially were thought to be pure dust and are in fact mixtures of dust with other types of particles.

For the rest of the analyzed period from April to September 2022 (classified as moderate events most in Fig. 8), most of the data falls into the region of large particle/BC mix and mixed dust/BC/BrC in Fig. 10. Since the UGR station is affected by local pollution, mainly road traffic, it is expected that the dust transported from the Saharan Desert gets mixed with the urban background pollution that is already suspended in the atmosphere. Another possibility is that dust already presents anthropogenic particles injected in the ensemble of particles during the transport process (Querol et al., 2019; Valenzuela et al., 2015). However, going further into the origin of these anthropogenic particles in the mixture is not possible with current data. To this study, the most important feature is that these possible mixtures can explain the differences in F$_{11}$ and -F$_{12}$/F$_{11}$ between the extreme and moderate dust events, and also the different situations of dust mixtures in the station.

To further understand the behavior of the optical properties during different dust events, we have performed an average of all moderate dust events of the period April-September 2022 (filtered by SAE < 0.5 to guarantee more dust predominance) and compared it with the peaks of the extreme dust events, i.e. 15th March 2022 at 17:00 UTC and 25th March 2022 at 09:00 UTC. To this purpose, Fig. 11 shows normalized

F_{11} and $-F_{12}/F_{11}$ phase matrix elements for the different situations. For comparisons, we also include laboratory measurements of Saharan dust samples with the polar nephelometer in the Andalusian Institute of Astrophysics (Muñoz et al., 2010), which are available in the Granada – Amsterdam Light Scattering Database (Muñoz et al., 2012). This database provides measurements of F_{11} and $-F_{12}/F_{11}$ at 488 and 632 nm (yellow dots in Fig. 11a,c) - see Gómez Martín et al., (2021) for details. Results of F_{11} have been normalized with respect to $F_{11}(30°)$ to have the same scale for comparison.
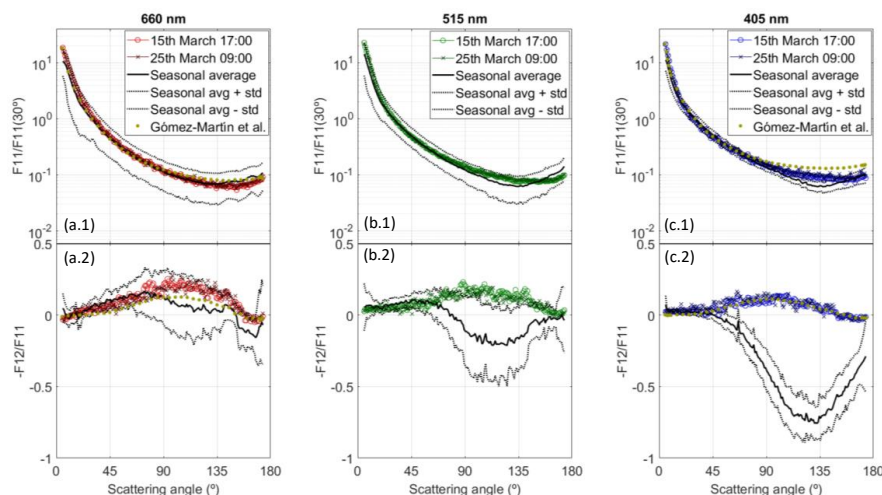
Figure 11. Phase function (F_{11}) (up) and polarized phase function ($-F_{12}/F_{11}$) (bottom) for different situations: Mean values for the cases obtained during moderate dust events (black lines), cases for extreme events on 15th March 2022 (red open circles) and on 25th March 2022 (red stars), and laboratory measurements (yellow dots) with samples collected in the Sahara and available in the Granada-Amsterdam Light Scattering database (Muñoz et al., 2012).

Figure 11 reveals that the F_{11} matrix element presents very similar features for the three wavelengths between mean averages for the period April-September 2022 and the extreme dust events, being the difference within the standard deviations. There are only slight differences in the forward region above 160° scattering angles, particularly for 515 nm channel, that might be associated by the complexity of the scattering at these angles for large and non-spherical particles (e.g. Mishchenko et al., 2002; Muñoz et al., 2007). Also, the small standard deviations of F_{11} are remarkable for the mean seasonal values, which suggest that F_{11} follows very similar patterns when there is predominance of big particles, independently of the mixture with other anthropogenic particles. Moreover, these patterns of F_{11} obtained from ambient aerosol basically coincide with the one provided by the Light Scattering Database.

The comparison of $-F_{12}/F_{11}$, however, reveals very important features. In all cases, seasonal values of $-F_{12}/F_{11}$ show much larger standard deviations when compared with F_{11} which suggests that $-F_{12}/F_{11}$ is more sensitive to the differences in the mixture of particles. Specifically, for 660 nm $-F_{12}/F_{11}$ follows a very similar pattern for the extreme events and the laboratory provided by the Granada-Amsterdam Light Scattering database and is characterized by the discussed bell-shape pattern with a maximum around 0.2 in the 100° scattering region. The mean seasonal average also follows the same pattern, but with a lower maximum and displaced to lower scattering regions. For the 515 nm channel the extreme dust cases show the classical bell shape with a maximum of 0.2 at 100° approximately, while for the average of usual dust cases there is a different pattern with values over zero up to 80°, decreasing later to the minimum values around -0.2 in the 100°-130° range and increasing again to values close to zero in the backward scattering region. Finally, the 405 nm channel is the one that presents the most different behavior between the seasonal averages and the phase matrix elements for the dust events with two different patterns: For the extreme dust events and the Light Scattering Database, there is a bell shape pattern with values close to zero and a maximum of 0.1 at 100°, being the differences between both sets of data negligible. The other pattern is observed for the mean average, characterized by values around zero up to 50°, decreasing later to

a minimum of -0.7 at 120° and increasing again to values close to 0 in the backward scattering region. We highlight that this last pattern in $-F_{12}/F_{11}$ is somehow like that observed for 515 nm but with an enhanced decrease and later increase in the region 120°-170°, which suggests that the 405 nm channel is more

595 sensitive to the presence of other particles of anthropogenic origin in the sampled air. Furthermore, the lower standard deviations observed for the 405 nm wavelength indicate homogeneity in the response to polarization, even in the presence of other anthropogenic particles in the sample.

The analysis of F_{11} and $-F_{12}/F_{11}$ phase matrix elements reveal that F_{11} patterns and spectral dependence is strongly affected by the existence of large and non-spherical particles, being the existence of other

600 anthropogenic particles in the mixture affecting mainly the backscattering region. However, the possible existence of anthropogenic particles in the ensemble of particles characterized by predominance of large and non-spherical particles can affect importantly the values of $-F_{12}/F_{11}$ with strong wavelength-dependence. These changes are critical in the UV wavelength being like the pattern observed for pollution and/or biomass-burning characterized by small and spherical particles (Bazo et al., 2024; Espinosa et al.,

605 2017). The visible and infrared channel show patterns more typical of pure dust measurements (Muñoz et al., 2007). Therefore, polarization measurements have a great potential for distinguishing different aerosol types in the mixture, which can be either internal or external mixtures of dust with other types of particles. Some model simulations even suggest that non-absorptive coating in mineral dust has a drastic variation in the behavior of $-F_{12}/F_{11}$ (Zhang et al., 2022, 2023), such as coatings of non-absorptive aerosol due to the

610 long-range transport (Dall'Osto et al., 2010). Future works will focus on detailed studies of chemical analyses in combination with polar nephelometry measurements to further exploit the potential of polarization measurements in aerosol studies.

3.2.4   Phase matrix simulations for different aerosol mixture scenarios

To fully understand how different degrees of mixture between anthropogenic particles and mineral dust can

615 affect F_{11} and $-F_{12}/F_{11}$, forward simulations with the Generalized Retrieval of Aerosol and Surface Properties algorithm (GRASP - Dubovik et al., 2014, 2021) have been performed. These simulations need inputs of different size distributions and refractive indexes to generate F_{11} and $-F_{12}/F_{11}$. Particularly, we used bi-lognormal size distribution, one representative of fine mode particles with modal radius of 0.15 μm and 0.25 μm of standard deviation and the other representative of coarse mode particles with modal radius

620 of 2.5 μm and 1 μm of standard deviation. Real refractive indexes were assumed non-spectrally dependent with values of 1.6 for fine mode and 1.55 for coarse mode. Imaginary refractive indexes were of 0.0015 for fine mode and with no spectral dependency, while for coarse mode there were of 0.007, 0.005 and 0.005 for 405, 515 and 660 nm. The sphere fraction was also fixed for each mode, being 0.7 for fine mode and 0.05 for coarse mode. This size distribution and refractive indexes can be considered representative of a

625 mixture of anthropogenic pollution and dust (e.g. Torres et al., 2017), and three different scenarios were generated giving different weights to each mode: The first is for volume concentrations of 0.3 μm³/μm³ for each mode and can be considered as representative of a mixed case where both modes have a similar weight. The second presents more predominance of coarse mode (volume concentrations of 0.5 μm³/μm³) but with non-negligible contribution of anthropogenic particles (volume concentrations of 0.1 μm³/μm³) in the fine

630 mode. The last scenario is representative of pure dust mode (volume concentrations of 0.5 μm³/μm³) with negligible fine mode contribution (volume concentrations of 0.01 μm³/μm³). Results of calculated of computed F_{11} and $-F_{12}/F_{11}$ are in Fig. 12.
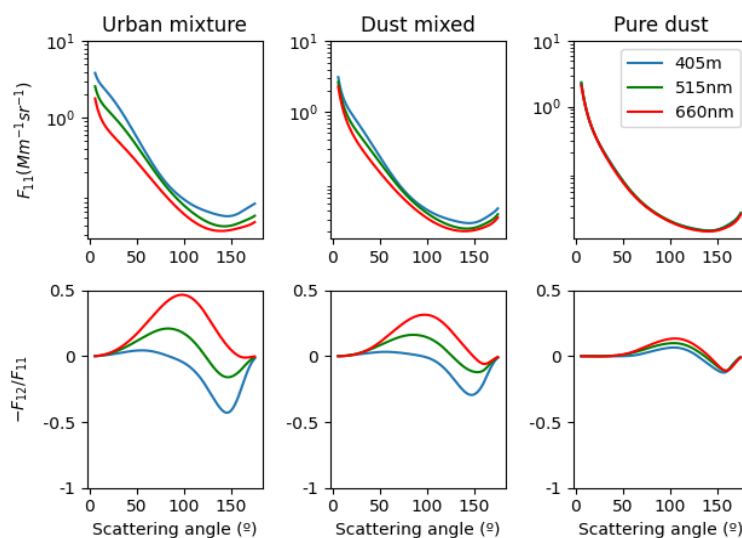
Figure 12. Simulations of phase function (F_{11}) and polarized phase function (-F_{12}/F_{11}) using GRASP forward for
635 **three different combinations of bi-lognormal size distributions.** *Urban Mixture* **with approximately the same**
weight of fine and coarse mode, *Dust mixed* **with predominance of coarse mode but with a non-negligible**
influence of the fine mode, and *Pure Dust* **with strong predominance of coarse mode and negligible fine mode.**
Note that refractive indexes and sphericity of each mode are different.

Figure 12 reveals different spectral important features in F_{11} and -F_{12}/F_{11} depending on the mixture. For F_{11},
640 the pattern is generally characterized by larger forward scattering with a minimum in the region of 120°-
150°, independently on the type of aerosol mixture and on wavelength. The largest spectral dependencies
are for the *Urban Mixture* case while for the other two cases such spectral dependencies become negligible.
However, for -F_{12}/F_{11} the largest variations in spectral dependencies and patterns are observed. In the *Urban
Mixture* case the 660 nm channel shows a bell-shape pattern with maximum of ~ 0.4 in the region around
645 100°, while for 405 nm -F_{12}/F_{11} shows approximately constants values close to zero until ~ 50° when it
starts to decrease until the minimum of -0.5 in the region ~140°. Later it recovers reaching zero at 180°. On
the other hand, for *Pure Dust* the -F_{12}/F_{11} spectral dependencies are almost negligible, and it is characterized
by a bell-shaped pattern with maximum around 0.2 in the region 110°-130°. For the *Dust mixed* the pattern
is in-between the previous ones.

650 Figure 12 results aid comprehending the distinct dust patterns observed in Fig. 11 and the temporal
evolutions of the extreme dust events. Anthropogenic particles can drastically alter the spectral
dependencies in -F_{12}/F_{11}, particularly in the UV channels. It is important to note that changes in refractive
indexes, particularly the imaginary part, may also contribute to these differences in -F_{12}/F_{11}. Variations in
the sphericity parameter also affects -F_{12}/F_{11} behaviors. Having more accurate information for the
655 experimental study cases discussed in these studies would require performing GRASP inversions, but to do
this GRASP needs to be optimized to a configuration capable of separating optical properties of fine and
coarse modes.

4 Conclusions

This work has focused on the analyses of phase matrix elements and optical properties during extreme
660 mineral dust intrusions that were registered at the UGR station (Southeastern Spain) during the year 2022.
The analyses differentiate between two different scenarios: the first is two extreme Saharan dust outbreaks
that happened on March and affected the entire Iberian Peninsula with extremely high values of PM_{10}
concentration (~1000 µgm⁻³). The second is a set of intermedia Saharan dust events with more moderate
concentrations usually around 100 µgm⁻³. The main novelty of the analyses are the measurements by the
665 multiwavelength Polarized Imaging Nephelometer (PI-Neph) developed by GRASP-Earth capable of
providing two aerosol scattering matrix elements (F_{11} and -F_{12}/F_{11}) for three different wavelengths (405,

515 and 660 nm) directly from ambient air. To our knowledge, these are the first measurements of this type for ambient mineral dust transported to southern Europe, highlighting the multiwavelength and polarization degree of these measurements on a continuous way.

670   The two extreme Saharan dust outbreaks happened on $15^{th} – 16^{th}$ and on $25^{th} – 26^{th}$ March 2022 were associated with intense low-pressure systems located in southern Algeria that favored the injection of dust in the upper layers in the atmosphere and posteriorly were transported to the Iberian Peninsula, producing extreme hourly PM_{10} concentrations. The peak values were 1800 μgm^{-3} and 690 μgm^{-3} for the $15^{th} – 16^{th}$ and $25^{th} – 26^{th}$ March, respectively. The first event was stronger, but even though both events registered daily

675   values way over the daily limit value of 50 μgm^{-3} delimited by the 2008/50/CE European Directive. The detailed temporal evolution analysis of F_{11} and $-F_{12}/F_{11}$ revealed important features: F_{11} did not show relevant changes with time showing the classical pattern for predominance of big and non-spherical particles characterized by high predominance of forward scattering and almost negligible wavelength differences. However, the patterns for $-F_{12}/F_{11}$ showed variability during the different stages of the dust

680   outbreaks: for 515 and 660 nm the $-F_{12}/F_{11}$ patterns were bell-shape centered around 100° scattering angles and slightly positive values always present, while for 405 nm this bell-shape pattern was present only for the moments of extreme predominance of dust. In the moments before the dust arrival and when it starts to withdraw, $-F_{12}/F_{11}$ for 405 nm shows a very different pattern with values close to zero up to 50° - 60°, followed by a decrease to values between -0.4 and -0.6 in the region around 120°, and an increase recovering

685   to values close to zero in the backward region. These patterns were further analyzed using additional instrumentation in the UGR station and concluded that the bell-shape patterns were typical for pure dust particles, where the others were associated with mixtures of dust particles urban background aerosol. This affected other intensive optical properties such as lidar ratio (LR) that provided typical values for dust (~45 sr^{-1}) during the peaks of intrusions and more variable values at other moments. Other extensive aerosol

690   optical properties such as the single scattering albedo (SSA) revealed differences between the peaks of the intrusions (0.98 - 0.83, depending on wavelength) when compared versus other moments with lower concentration (values between 0.87 - 0.72).

The continuous operation of the PI-Neph combined with measurements of other instruments for the extensive period April – September 2022 allowed the analysis of the impact of the typical Saharan dust

695   intrusions that affected the UGR station. We differentiated these intrusions from the previous two extreme events because they registered maximum PM_{10} around 100 μgm^{-3}, which are more typical values for Saharan dust outbreaks in the UGR station. Data selection was done by keeping only data with scattering Angström Exponent below 1.0. This allowed to include a large variety of situations reflected in the variability of extensive parameters such as SSA or LR. The combination of scattering and absorption

700   measurements classified most of the data for this entire period as mixture of dust particles with other anthropogenic aerosol particles. The analysis of F_{11} and $-F_{12}/F_{11}$ revealed again important features. F_{11} mostly followed the classical pattern characterized by strong forward scattering, although some cases showed some spectral dependence on 405 nm depending on the influence of fine mode particles in the mixture. However, the analysis of $-F_{12}/F_{11}$ revealed big differences among wavelengths, being 405 nm

705   characterized by a well-defined pattern with values close to zero up to 50°-60° and negative values for the rest of scattering angles, while for the other channels at 515 and 660 nm they show a bell-shape pattern but with noise probably associated with the different influences of fine mode particles.

Laboratory measurements of mineral dust samples available in the Granada-Amsterdam Light Scattering Database allowed a comparative assessment of the different Saharan dust outbreaks that affected the UGR

710   station. To that end, averages of the period April – September 2022 plus the peaks of the extreme events during March 2022 were used. For comparisons, F_{11} were normalized with respect to $F_{11}(30°)$. The results showed that for all F_{11} the differences between temporal averages, peak events and laboratory measurements were minimal, being only notable in the backscattering region close to 180°. For $-F_{12}/F_{11}$ laboratory measurements and extreme events measurements (peak of concentration) agree quite well both

715   for 405 and 660 nm, being the differences within the uncertainties. However, when comparing with the seasonal averages for the period April – September some important features are revealed: for 660 nm it seems to reproduce the same pattern than for laboratory/extreme event measurements, although with large standard deviations when compared with other wavelengths. But for 405 nm the seasonal mean has a very distinct pattern characterized again by values close to zero in the region up to 50°-60° and negative values

720   for the rest of angles. Standard deviations are now considerably lower. The channel at 515 nm shows an

intermedia situation. Considering that laboratory measurements consist of pure dust samples directly collected in the dessert, we can conclude that the $-F_{12}/F_{11}$ measured in the laboratory is only reproduced when there are extreme concentrations of dust in the atmosphere, while when there is more contribution of anthropogenic particles in the mixture it affects critically to $-F_{12}/F_{11}$ in the 405 nm channel. For the other

725 channels, particularly 660 nm, $-F_{12}/F_{11}$ seems to be less critically affected by the contribution of anthropogenic particles. Simulations performed by the GRASP code for different mixtures of fine mode anthropogenic particles and dust particles associated with the coarse mode revealed that F_{11} and $-F_{12}/F_{11}$ are sensitive to the different contribution of each mode in the mixture, being especially critical for $-F_{12}/F_{11}$ in the UV channel. Further optimizations of GRASP will allow retrievals for each case, differentiating

730 between fine and coarse mode optical and microphysical properties.

Measurements of F_{11} and $-F_{12}/F_{11}$ phase matrix elements for ambient aerosols have allowed a comprehensive analysis of the different dust events and reveals the capacity of polarization measurements for further investigating mineral dust particles in the atmosphere, particularly in determining the presence of other particles of anthropogenic origin in the mixture. However, going further in understanding the

735 interaction of dust with these anthropogenic particles requires of further analyses that provide the chemical composition of the ensemble of particles and the final composition and shape of the particles after interacting. This is planned in future studies that will allow a more complete comprehensive analysis. We therefore believe that multiwavelength polarized polar nephelometry opens new possibilities in the studies of mineral dust role in the climate system.

740

Competing Interests

The contact author has declared that none of the authors has any competing interests

Acknowledgments

745 This work was supported by the Junta de Andalucía Excellence project ADAPNE (P20-00136), AEROPRE (P-18-RT-3820), the European Union's Horizon 2020 research and innovation program through projects HORIZON-MSCA-2022-SE-01-01 (grant agreement No 101131631), ACTRIS.IMP (grant agreement No 871115) and ATMO_ACCESS (grant agreement No 101008004), by the Spanish Ministry of Science and Innovation through projects ELPIS (PID2020-12001-5RB-I00), EQC2019 006423-P, MULHACEN

750 (PID2021-128008OB-I00), NUCLEUS (PID2021-128757OB-I00) funded by MICIU/AEI/10.13039/501100011033 and by ERDF A way of making Europe, and ACTRIS-España (RED2022-134824-E), and by University of Granada Plan Propio through Excellence Research Unit Earth Science and Singular Laboratory AGORA (LS2022-1) programs. E. Bazo received funding by MICIU/AEI/10.13039/501100011033 and the ESF + through FPI fellowship PRE2022-101272. F.J.

755 García-Izquierdo acknowledges financial support from the grant PID2021-123370OB-I00 (CATS) funded by MCIN/AEI/10.13039/501100011033.

References

760 Adebiyi, A. A., & Kok, J. F. Climate models miss most of the coarse dust in the atmosphere. *Sci. Adv.*, *6*(15). https://doi.org/10.1126/sciadv.aaz9507, 2020.

Adebiyi, A.A., Huang, Y., Samset, B.H. and Kok, J. F. Observations suggest that North African dust absorbs less solar radiation than models estimate. *Commun. Earth Environ.* 4, 168. https://doi.org/10.1038/s43247-023-00825-2, 2023.

765 Anderson, T. L., Covert, D. S., Marshall, S. F., Laucks, M. L., Charlson, R. J., Waggoner, A. P., Ogren, J. A., Caldow, R., Holm, R. L., Quant, F. R., Sem, G. J., Wiedensohler, A., Ahlquist, N. A., & Bates, T. S. Performance Characteristics of a High-Sensitivity, Three-Wavelength, Total Scatter/Backscatter Nephelometer. *J. Atmos. Ocean. Technol.*, *13*(5), 967–986. https://doi.org/10.1175/1520-0426(1996)013<0967:PCOAHS>2.0.CO;2, 1996.

770   Anderson, T. L., & Ogren, J. A. Determining Aerosol Radiative Properties Using the TSI 3563 Integrating Nephelometer. *Aerosol Sci. Tech.*, *29*(1), 57–69. https://doi.org/10.1080/02786829808965551, 1998.

Bazo, E., Granados-Muñoz, M. J., Román, R., Bravo-Aranda, J. A., Cazorla, A., Valenzuela, A., González, R., Olmo, F. J., & Alados-Arboledas, L. Evaluation of the vertically-resolved aerosol

775   radiative effect on shortwave and longwave ranges using sun-sky photometer and ceilometer measurements. *Atmos. Res.*, *282*. https://doi.org/10.1016/j.atmosres.2022.106517, 2023.

Bazo, E., Martins, J. V., Perez-Ramirez, D., Valenzuela, A., Titos, G., Cazorla, A., Fuertes, D., Weiss, M., Turpie, A., Li, C., García-Izquierdo, F. J., Foyo-Moreno, I., Alados-Arboledas, L., & Olmo, F. J. Optimization of the Polarized Imaging Nephelometer (PI-Neph) for continuous monitoring

780   of multiwavelength aerosol phase functions in support of space polarimetry missions. *Atmos. Environ.*, *316*, 120181. https://doi.org/10.1016/j.atmosenv.2023.120181, 2024.

Benedetti, A., Morcrette, J. -J., Boucher, O., Dethof, A., Engelen, R. J., Fisher, M., Flentje, H., Huneeus, N., Jones, L., Kaiser, J. W., Kinne, S., Mangold, A., Razinger, M., Simmons, A. J., & Suttie, M. Aerosol analysis and forecast in the European Centre for Medium-Range Weather

785   Forecasts Integrated Forecast System: 2. Data assimilation. *J. Geophys. Res.*, *114*(D13). https://doi.org/10.1029/2008JD011115, 2009.

Casquero-Vera, J.A., Lyamani, H., Titos, G., Minguillón, M.C., Dada, L., Alastuey, A., Querol, X., Petäjä, T., Olmo, F.J. and Alados-Arboledas, L. Quantifying traffic, biomass burning and secondary source contributions to atmospheric particle number concentrations at urban and

790   suburban sites, *Sci. Tot. Environ.*, 768, 145282, https://doi.org/10.1016/j.scitotenv.2021.145282, 2021.

Cazorla, A., Bahadur, R., Suski, K. J., Cahill, J. F., Chand, D., Schmid, B., Ramanathan, V., & Prather, K. A. Relating aerosol absorption due to soot, organic carbon, and dust to emission sources determined from in-situ chemical measurements. *Atmos. Chem. Phys.*, *13*(18), 9337–

795   9350. https://doi.org/10.5194/acp-13-9337-2013, 2013.

Cazorla, A., Casquero-Vera, J. A., Román, R., Guerrero-Rascado, J. L., Toledano, C., Cachorro, V. E., Orza, J. A. G., Cancillo, M. L., Serrano, A., Titos, G., Pandolfi, M., Alastuey, A., Hanrieder, N., & Alados-Arboledas, L. Near-real-time processing of a ceilometer network assisted with sun-photometer data: monitoring a dust outbreak over the Iberian Peninsula. *Atmos. Chem.*

800   *Phys.*, *17*(19), 11861–11876. https://doi.org/10.5194/acp-17-11861-2017, 2017.

Cuevas-Agulló, E., Barriopedro, D., García, R. D., Alonso-Pérez, S., González-Alemán, J. J., Werner, E., Suárez, D., Bustos, J. J., García-Castrillo, G., García, O., Barreto, Á., and Basart, S. Sharp increase in Saharan dust intrusions over the western Euro-Mediterranean in February–March 2020–2022 and associated atmospheric circulation, *Atmos. Chem. Phys.*, 24, 4083–4104,

805   https://doi.org/10.5194/acp-24-4083-2024, 2024.

Curtis, D. B., Meland, B., Aycibin, M., Arnold, N. P., Grassian, V. H., Young, M. A., & Kleiber, P. D. A laboratory investigation of light scattering from representative components of mineral dust aerosol at a wavelength of 550 nm. *J. Geophys. Res.*, *113*(8). https://doi.org/10.1029/2007JD009387, 2008.

810   Dall'Osto, M., Harrison, R. M., Highwood, E. J., O'Dowd, C., Ceburnis, D., Querol, X., & Achterberg, E. P. Variation of the mixing state of Saharan dust particles with atmospheric transport. *Atmos. Environ.*, *44*(26), 3135–3146. https://doi.org/10.1016/j.atmosenv.2010.05.030, 2010.

Di Biagio, C., Formenti, P., Balkanski, Y., Caponi, L., Cazaunau, M., Pangui, E., Journet, E., Nowak,

815   S., Andreae, M. O., Kandler, K., Saeed, T., Piketh, S., Seibert, D., Williams, E., & Doussin, J. F. Complex refractive indices and single-scattering albedo of global dust aerosols in the shortwave spectrum and relationship to size and iron content. *Atmos. Chem. Phys.*, *19*(24), 15503–15531. https://doi.org/10.5194/acp-19-15503-2019, 2019.

820   Di Biagio, C., Formenti, P., Balkanski, Y., Caponi, L., Cazaunau, M., Pangui, E., Journet, E., Nowak, S., Caquineau, S., Andreae, M. O., Kandler, K., Saeed, T., Piketh, S., Seibert, D., Williams, E., & Doussin, J.-F. Global scale variability of the mineral dust long-wave refractive index: a new dataset of in situ measurements for climate modeling and remote sensing. *Atmos. Chem. Phys.*, *17*(3), 1901–1929. https://doi.org/10.5194/acp-17-1901-2017, 2017.

825   Dolgos, G., & Martins, J. V. Polarized Imaging Nephelometer for in situ airborne measurements of aerosol light scattering. *Opt. Express*, *22*(18), 21972. https://doi.org/10.1364/OE.22.021972, 2014.

Drinovec, L., Močnik, G., Zotter, P., Prévôt, A. S. H., Ruckstuhl, C., Coz, E., Rupakheti, M., Sciare, J., Müller, T., Wiedensohler, A., & Hansen, A. D. A. The "dual-spot" Aethalometer: an improved measurement of aerosol black carbon with real-time loading
830   compensation. *Atmos. Meas. Tech.*, *8*(5), 1965–1979. https://doi.org/10.5194/amt-8-1965-2015, 2015.

Dubovik, O., Fuertes, D., Litvinov, P., Lopatin, A., Lapyonok, T., Doubovik, I., Xu, F., Ducos, F., Chen, C., Torres, B., Derimian, Y., Li, L., Herreras-Giralda, M., Herrera, M., Karol, Y., Matar, C., Schuster, G. L., Espinosa, R., Puthukkudy, A., … Federspiel, C. A Comprehensive
835   Description of Multi-Term LSM for Applying Multiple a Priori Constraints in Problems of Atmospheric Remote Sensing: GRASP Algorithm, Concept, and Applications. *Front. Remote Sens.*, *2*. https://doi.org/10.3389/frsen.2021.706851, 2021.

Dubovik, O., Herman, M., Holdak, A., Lapyonok, T., Tanré, D., Deuzé, J. L., Ducos, F., Sinyuk, A., and Lopatin, A.: Statistically optimized inversion algorithm for enhanced retrieval of aerosol
840   properties from spectral multi-angle polarimetric satellite observations, *Atmos. Meas. Tech.*, 4, 975–1018, https://doi.org/10.5194/amt-4-975-2011, 2011.

Dubovik, O., Holben, B., Eck, T. F., Smirnov, A., Kaufman, Y. J., King, M. D., Tanré, D., & Slutsker, I. Variability of Absorption and Optical Properties of Key Aerosol Types Observed in Worldwide Locations. *J. Atmos. Sci.*, *59*(3), 590–608. https://doi.org/10.1175/1520-
845   0469(2002)059<0590:VOAAOP>2.0.CO;2, 2002.

Dubovik, O., Lapyonok, T., Litvinov, P., Herman, M., Fuertes, D., Ducos, F., Lopatin, A., Chaikovsky, A., Torres, B., Derimian, Y., Huang, X., Aspetsberger, M., & Federspiel, C. GRASP: a versatile algorithm for characterizing the atmosphere. *SPIE Newsroom*. https://doi.org/10.1117/2.1201408.005558, 2014.

850   Dubovik, O., Sinyuk, A., Lapyonok, T., Holben, B. N., Mishchenko, M., Yang, P., Eck, T. F., Volten, H., Muñoz, O., Veihelmann, B., van der Zande, W. J., Leon, J.-F., Sorokin, M., & Slutsker, I. Application of spheroid models to account for aerosol particle nonsphericity in remote sensing of desert dust. *J. Geophys. Res.,* 111(D11). https://doi.org/https://doi.org/10.1029/2005JD006619, 2006.

855   Gonçalves Ageitos, M., Obiso, V., Miller, R. L., Jorba, O., Klose, M., Dawson, M., Balkanski, Y., Perlwitz, J., Basart, S., Di Tomaso, E., Escribano, J., Macchia, F., Montané, G., Mahowald, N. M., Green, R. O., Thompson, D. R., and Pérez García-Pando, C. Modeling dust mineralogical composition: sensitivity to soil mineralogy atlases and their expected climate impacts, *Atmos. Chem. Phys.*, 23, 8623–8657, https://doi.org/10.5194/acp-23-8623-2023, 2023.

860   González-Flórez, C., Klose, M., Alastuey, A., Dupont, S., Escribano, J., Etyemezian, V., Gonzalez-Romero, A., Huang, Y., Kandler, K., Nikolich, G., Panta, A., Querol, X., Reche, C., Yus-Díez, J., and Pérez García-Pando, C. Insights into the size-resolved dust emission from field measurements in the Moroccan Sahara, *Atmos. Chem. Phys.*, 23, 7177–7212, https://doi.org/10.5194/acp-23-7177-2023, 2023.

865   González-Romero, A., González-Flórez, C., Panta, A., Yus-Díez, J., Reche, C., Córdoba, P., Moreno, N., Alastuey, A., Kandler, K., Klose, M., Baldo, C., Clark, R. N., Shi, Z., Querol, X., and Pérez García-Pando, C. Variability in sediment particle size, mineralogy, and Fe mode of occurrence

across dust-source inland drainage basins: the case of the lower Drâa Valley, Morocco, *Atmos. Chem. Phys.*, 23, 15815–15834, https://doi.org/10.5194/acp-23-15815-2023, 2023.

Escudero, M., Castillo, S., Querol, X., Avila, A., Alarcón, M., Viana, M. M. M., Alastuey, A., Cuevas, E., & Rodríguez, S. Wet and dry African dust episodes over eastern Spain. *J. Geophys. Res.*, *110*(D18). https://doi.org/10.1029/2004JD004731, 2005.

Espinosa, W. R., Martins, J. V., Remer, L. A., Dubovik, O., Lapyonok, T., Fuertes, D., Puthukkudy, A., Orozco, D., Ziemba, L., Thornhill, K. L., & Levy, R. Retrievals of Aerosol Size Distribution, Spherical Fraction, and Complex Refractive Index From Airborne In Situ Angular Light Scattering and Absorption Measurements. *J. Geophys. Res.*, *124*(14), 7997–8024. https://doi.org/10.1029/2018JD030009, 2019.

Espinosa, W. R., Martins, J. V., Remer, L. A., Puthukkudy, A., Orozco, D., & Dolgos, G. In situ measurements of angular-dependent light scattering by aerosols over the contiguous United States. *Atmos. Chem. Phys.*, *18*(5), 3737–3754. https://doi.org/10.5194/acp-18-3737-2018, 2018.

Espinosa, W. R., Remer, L. A., Dubovik, O., Ziemba, L., Beyersdorf, A., Orozco, D., Schuster, G., Lapyonok, T., Fuertes, D., & Martins, J. V. Retrievals of aerosol optical and microphysical properties from Imaging Polar Nephelometer scattering measurements. *Atmos. Meas. Tech.*, *10*(3), 811–824. https://doi.org/10.5194/amt-10-811-2017, 2017.

Fan, J., Wang, Y., Rosenfeld, D., & Liu, X. Review of Aerosol–Cloud Interactions: Mechanisms, Significance, and Challenges. *J. Atmos. Sci.*, *73*(11), 4221–4252. https://doi.org/10.1175/JAS-D-16-0037.1, 2016.

Fernández, A. J., Sicard, M., Costa, M. J., Guerrero Rascado, J., Gomez, J., Molero, F., Barragán, R., Basart, S., Bortoli, D., Bedoya-Velásquez, A., & et al. Extreme, wintertime Saharan dust intrusion in the Iberian Peninsula: lidar monitoring and evaluation of dust forecast models during the February 2017 event. *Atmos. Res.*, *228*, 223–241. https://doi.org/10.1016/j.atmosres.2019.06.007, 2019.

Formenti, P., Caquineau, S., Desboeufs, K., Klaver, A., Chevaillier, S., Journet, E., & Rajot, J. L. Mapping the physico-chemical properties of mineral dust in western Africa: mineralogical composition. *Atmos. Chem. Phys.*, *14*(19), 10663–10686. https://doi.org/10.5194/acp-14-10663-2014, 2014.

Formenti, P., Elbert, W., Maenhaut, W., Haywood, J., & Andreae, M. O. Chemical composition of mineral dust aerosol during the Saharan Dust Experiment (SHADE) airborne campaign in the Cape Verde region, September 2000. *J. Geophys. Res.*, *108*(18). https://doi.org/10.1029/2002jd002648, 2003.

Forster, P. ., Storelvmo, T. ., Armour, K. ., Collins, W. ., Dufresne, J.-L. ., Frame, D. ., Lunt, D. J. ., Mauritsen, T. ., Palmer, M. D. ., Watanabe, M. ., Wild, M. ., & Zhang, H. The Earth's Energy Budget, Climate Feedbacks, and Climate Sensitivity. In V. Masson-Delmotte, P. Zhai, A. Pirani, S. L. Connors, C. Péan, S. Berger, N. Caud, Y. Chen, L. Goldfarb, M. I. Gomis, M. Huang, K. Leitzell, E. Lonnoy, J. B. R. Matthews, T. K. Maycock, T. Waterfield, O. Yelekçi, R. Yu, & B. Zhou (Eds.), *Climate Change 2021: The Physical Science Basis. Contribution of Working Group I to the Sixth Assessment Report of the Intergovernmental Panel on Climate Change* (pp. 953–1054). Cambridge University Press, 2021.

Gómez Martín, J. C., Guirado, D., Frattin, E., Bermudez-Edo, M., Cariñanos Gonzalez, P., Olmo Reyes, F. J., Nousiainen, T., Gutiérrez, P. J., Moreno, F., & Muñoz, O. On the application of scattering matrix measurements to detection and identification of major types of airborne aerosol particles: Volcanic ash, desert dust and pollen. *J. Quant. Spectrosc. Radiat. Transf.*, *271*. https://doi.org/10.1016/j.jqsrt.2021.107761, 2021.

915   Groß, S., Esselborn, M., Weinzierl, B., Wirth, M., Fix, A., & Petzold, A. Aerosol classification by airborne high spectral resolution lidar observations. *Atmos. Chem. Phys.*, *13*(5), 2487–2505. https://doi.org/10.5194/acp-13-2487-2013, 2013.

Guerrero-Rascado, J. L., Olmo, F. J., Avilés-Rodríguez, I., Navas-Guzmán, F., Pérez-Ramírez, D., Lyamani, H., & Alados Arboledas, L. Extreme Saharan dust event over the southern Iberian
920   Peninsula in september 2007: active and passive remote sensing from surface and satellite. *Atmos. Chem. Phys.*, *9*(21), 8453–8469. https://doi.org/10.5194/acp-9-8453-2009, 2009.

Haywood, J., and Boucher, O. Estimates of the direct and indirect radiative forcing due to tropospheric aerosols: A review, *Rev. Geophys.*, 38(4), 513–543, https://doi.org/10.1029/1999RG000078, 2000.

925   Horvath, H., Alados Arboledas, L., & José Olmo Reyes, F. Angular scattering of the Sahara dust aerosol. *Atmos. Chem. Phys.*, *18*(23), 17735–17744. https://doi.org/10.5194/acp-18-17735-2018, 2018.

Huang, Y., Kok, J. F., Martin, R. L., Swet, N., Katra, I., Gill, T. E., Reynolds, R. L., & Freire, L. S. Fine dust emissions from active sands at coastal Oceano Dunes, California. *Atmos. Chem.*
930   *Phys.*, *19*(5), 2947–2964. https://doi.org/10.5194/acp-19-2947-2019, 2019.

Huang, Y., Liu, C., Yao, B., Yin, Y., & Bi, L. Scattering matrices of mineral dust aerosols: A refinement of the refractive index impact. *Atmos. Chem. Phys.*, *20*(5), 2865–2876. https://doi.org/10.5194/acp-20-2865-2020, 2020.

Kalnay, E., Kanamitsu, M., Kistler, R., Collins, W., Deaven, D., Gandin, L., Iredell, M., Saha, S.,
935   White, G., Woollen, J., Zhu, Y., Leetmaa, A., Reynolds, R., Chelliah, M., Ebisuzaki, W., Higgins, W., Janowiak, J., Mo, K. C., Ropelewski, C., … Joseph, D. The NCEP/NCAR 40-Year Reanalysis Project. *Bull. Am. Meteorol. Soc.*, *77*(3), 437–471. https://doi.org/10.1175/1520-0477(1996)077<0437:TNYRP>2.0.CO;2, 1996.

Kanamitsu, M., Ebisuzaki, W., Woollen, J., Yang, S.-K., Hnilo, J. J., Fiorino, M., & Potter, G. L.
940   NCEP–DOE AMIP-II Reanalysis (R-2). *Bull. Am. Meteorol. Soc.*, *83*(11), 1631–1644. https://doi.org/10.1175/BAMS-83-11-1631, 2002.

Kok, J. F., Adebiyi, A. A., Albani, S., Balkanski, Y., Checa-Garcia, R., Chin, M., Colarco, P. R., Hamilton, D. S., Huang, Y., Ito, A., Klose, M., Leung, D. M., Li, L., Mahowald, N. M., Miller, R. L., Obiso, V., Pérez García-Pando, C., Rocha-Lima, A., Wan, J. S., & Whicker, C. A.
945   Improved representation of the global dust cycle using observational constraints on dust properties and abundance. *Atmos. Chem. Phys.*, *21*(10), 8127–8167. https://doi.org/10.5194/acp-21-8127-2021, 2021.

Kok, J. F., Ridley, D. A., Zhou, Q., Miller, R. L., Zhao, C., Heald, C. L., Ward, D. S., Albani, S., & Haustein, K. Smaller desert dust cooling effect estimated from analysis of dust size and
950   abundance. *Nat. Geosci.10*(4), 274–278. https://doi.org/10.1038/ngeo2912, 2017.

Kok, J. F., Ward, D. S., Mahowald, N. M., & Evan, A. T. Global and regional importance of the direct dust-climate feedback. *Nat. Commun. 9*(1), 241. https://doi.org/10.1038/s41467-017-02620-y, 2018.

Leskinen, J., Hartikainen, A., Väätäinen, S., Ihalainen, M., Virkkula, A., Mesceriakovas, A., Tiitta,
955   P., Miettinen, M., Lamberg, H., Czech, H., Yli-Pirilä, P., Tissari, J., Jakobi, G., Zimmermann, R. and Sippula O. Photochemical Aging Induces Changes in the Effective Densities, Morphologies, and Optical Properties of Combustion Aerosol Particles. *Environ. Sci. Technol.* 57, 5137–5148. https://doi.org/10.1021/acs.est.2c04151, 2023.

Liu, J., Zhang, Q., Wang, J., & Zhang, Y. Light scattering matrix for soot aerosol: Comparisons
960   between experimental measurements and numerical simulations. *J. Quant. Spectrosc. Radiat. Transf.*, *246*. https://doi.org/10.1016/j.jqsrt.2020.106946, 2020.

Lyamani, H., Olmo, F. J., & Alados-Arboledas, L. Physical and optical properties of aerosols over an urban location in Spain: seasonal and diurnal variability. *Atmos. Chem. Phys.*, *10*(1), 239–254. https://doi.org/10.5194/acp-10-239-2010, 2010.

965   Lyamani, H., Fernández-Gálvez, J., Pérez-Ramírez, D., Valenzuela, A., Antón, M., Alados, I., Titos, G., Olmo, F.J. and Alados-Arboledas, L. Aerosol properties over two urban sites in South Spain during an extended stagnation episode in winter season, *Atmos. Environ.*, 62, 424-432. https://doi.org/10.1016/j.atmosenv.2012.08.050, 2012.

Meland, B., Kleiber, P. D., Grassian, V. H., & Young, M. A. Correlated IR spectroscopy and visible
970   light scattering measurements of mineral dust aerosol. *J. Geophys. Res.*, *115*(20). https://doi.org/10.1029/2010JD014389, 2010.

Mishchenko, M. I., Travis, L. D., & Lacis, A. A. *Scattering, Absorption, and Emission of Light by Small Particles*. Cambridge University Press, 2002.

Moallemi, A., Modini, R. L., Brem, B. T., Bertozzi, B., Giaccari, P., and Gysel-Beer, M.: Concept,
975   absolute calibration, and validation of a new benchtop laser imaging polar nephelometer, *Atmos. Meas. Tech.*, 16, 3653–3678, https://doi.org/10.5194/amt-16-3653-2023, 2023.

Moallemi, A., Modini, R. L., Lapyonok, T., Lopatin, A., Fuertes, D., Dubovik, O., Giaccari, P., and Gysel-Beer, M.: Information content and aerosol property retrieval potential for different types of in situ polar nephelometer data, *Atmos. Meas. Tech.*, 15, 5619–5642,
980   https://doi.org/10.5194/amt-15-5619-2022, 2022.

Morcrette, J. -J., Boucher, O., Jones, L., Salmond, D., Bechtold, P., Beljaars, A., Benedetti, A., Bonet, A., Kaiser, J. W., Razinger, M., Schulz, M., Serrar, S., Simmons, A. J., Sofiev, M., Suttie, M., Tompkins, A. M., & Untch, A. Aerosol analysis and forecast in the European Centre for Medium-Range Weather Forecasts Integrated Forecast System: Forward modeling. *J. Geophys.*
985   *Res.*, *114*(D6). https://doi.org/10.1029/2008JD011235, 2009.

Müller, D., Ansmann, A., Mattis, I., Tesche, M., Wandinger, U., Althausen, D., & Pisani, G. Aerosol-type-dependent lidar ratios observed with Raman lidar. *J. Geophys. Res.*, *112*(D16). https://doi.org/10.1029/2006JD008292, 2007.

Muñoz, O., Moreno, F., Guirado, D., Dabrowska, D. D., Volten, H., & Hovenier, J. W. The
990   Amsterdam–Granada Light Scattering Database. *J. Quant. Spectrosc. Radiat. Transf.*, *113*(7), 565–574. https://doi.org/10.1016/j.jqsrt.2012.01.014, 2012.

Muñoz, O., Moreno, F., Guirado, D., Ramos, J. L., López, A., Girela, F., Jerónimo, J. M., Costillo, L. P., & Bustamante, I. Experimental determination of scattering matrices of dust particles at visible wavelengths: The IAA light scattering apparatus. *J. Quant. Spectrosc. Radiat. Transf.*,
995   *111*(1), 187–196. https://doi.org/10.1016/j.jqsrt.2009.06.011, 2010.

Muñoz, O., Volten, H., Hovenier, J. W., Nousiainen, T., Muinonen, K., Guirado, D., Moreno, F., & Waters, L. B. F. M. Scattering matrix of large Saharan dust particles: Experiments and computations. *J. Geophys. Res.*, *112*(13). https://doi.org/10.1029/2006JD008074, 2007.

Ooki, A., & Uematsu, M. (2005). Chemical interactions between mineral dust particles and acid gases
1000   during Asian dust events. *J. Geophys. Res.*, *110*(D3). https://doi.org/10.1029/2004JD004737

Párraga, J., Martín-García, J. M., Delgado, G., Molinero-García, A., Cervera-Mata, A., Guerra, I., Fernández-González, M. V., Martín-Rodríguez, F. J., Lyamani, H., Casquero-Vera, J. A., Valenzuela, A., Olmo, F. J., & Delgado, R. Intrusions of dust and iberulites in Granada basin (Southern Iberian Peninsula). Genesis and formation of atmospheric iberulites. *Atmos. Res.*,
1005   *248*, 105260. https://doi.org/10.1016/j.atmosres.2020.105260, 2021.

Patrón, D., Lyamani, H., Titos, G., Casquero-Vera, J. A., Cardell, C., Močnik, G., Alados-Arboledas, L., & Olmo, F. J. Monumental heritage exposure to urban black carbon pollution. *Atmos. Environ.*, *170*, 22–32. https://doi.org/10.1016/J.ATMOSENV.2017.09.030, 2017.

1010   Pérez-Ramírez, D., Lyamani, H., Olmo, F. J., Whiteman, D. N., and Alados-Arboledas, L. Columnar aerosol properties from sun-and-star photometry: statistical comparisons and day-to-night dynamic, *Atmos. Chem. Phys.*, 12, 9719–9738, https://doi.org/10.5194/acp-12-9719-2012, 2012.

1015   Pérez-Ramírez, D., Lyamani, H., Smirnov, A., O´Neill, N. T., Veselovskii, I., Whiteman, D. N., Olmo, F. J., & Alados-Arboledas, L. Statistical study of day and night hourly patterns of columnar aerosol properties using sun and star photometry, *SPIE Remote Sensing*, https://doi.org/10.1117/12.2242372, 2016.

Petzold, A., and Schönlinner, M. Multi-angle absorption photometry—a new method for the measurement of aerosol light absorption and atmospheric black carbon. *J. Aerosol Sci.*, *35*(4), 421–441. https://doi.org/10.1016/J.JAEROSCI.2003.09.005, 2004.

1020   Querol, X., Pérez, N., Reche, C., Ealo, M., Ripoll, A., Tur, J., Pandolfi, M., Pey, J., Salvador, P., Moreno, T., & Alastuey, A. African dust and air quality over Spain: Is it only dust that matters? *Sci. Tot. Environ.,* 686, 737–752. https://doi.org/10.1016/j.scitotenv.2019.05.349, 2019.

Rodríguez, S. and López-Darias, J. Emerging extreme Saharan-dust events expand northward over the Atlantic and Europe prompting record-breaking PM10 and PM2.5 episodes, EGUsphere
1025   [preprint], https://doi.org/10.5194/egusphere-2023-3083, 2024.

Rosenfeld, D., Andreae, M. O., Asmi, A., Chin, M., de Leeuw, G., Donovan, D. P., Kahn, R., Kinne, S., Kivekäs, N., Kulmala, M., Lau, W., Schmidt, K. S., Suni, T., Wagner, T., Wild, M., & Quaas, J. Global observations of aerosol-cloud-precipitation-climate interactions. *Rev. Geophys.*, *52*(4), 750–808. https://doi.org/10.1002/2013RG000441, 2014.

1030   Salvador, P., Alonso-Pérez, S., Pey, J., Artíñano, B., de Bustos, J. J., Alastuey, A., & Querol, X. African dust outbreaks over the western Mediterranean Basin: 11-year characterization of atmospheric circulation patterns and dust source areas. *Atmos. Chem. Phys.*, *14*(13), 6759–6775. https://doi.org/10.5194/acp-14-6759-2014, 2014.

Schmeisser, L., Andrews, E., Ogren, J. A., Sheridan, P., Jefferson, A., Sharma, S., Kim, J. E.,
1035   Sherman, J. P., Sorribas, M., Kalapov, I., Arsov, T., Angelov, C., Mayol-Bracero, O. L., Labuschagne, C., Kim, S.-W., Hoffer, A., Lin, N.-H., Chia, H.-P., Bergin, M., … Wu, H. Classifying aerosol type using in situ surface spectral aerosol optical properties. *Atmos. Chem. Phys.*, *17*(19), 12097–12120. https://doi.org/10.5194/acp-17-12097-2017, 2017.

Teri, M., Gasteiger, J., Heimerl, K., Dollner, M., Schöberl, M., Seibert, P., Tipka, A., Müller, T.,
1040   Aryasree, S., Kandler, K., and Weinzierl, B. Pollution affects Arabian and Saharan dust optical properties in the Eastern Mediterranean, EGUsphere [preprint], https://doi.org/10.5194/egusphere-2024-701, 2024.

Titos, G., del Águila, A., Cazorla, A., Lyamani, H., Casquero-Vera, J. A., Colombi, C., Cuccia, E., Gianelle, V., Močnik, G., Alastuey, A., Olmo, F. J., & Alados-Arboledas, L. Spatial and
1045   temporal variability of carbonaceous aerosols: Assessing the impact of biomass burning in the urban environment. *Sci. Tot. Environ.*, *578*, 613–625. https://doi.org/https://doi.org/10.1016/j.scitotenv.2016.11.007, 2017.

Titos, G., Lyamani, H., Pandolfi, M., Alastuey, A., & Arboledas, L. Identification of fine (PM 1) and coarse (PM 10-1) sources of particulate matter in an urban environment. *Atmos. Environ.*, *89*,
1050   593–602. https://doi.org/10.1016/j.atmosenv.2014.03.001, 2014.

Torres, B., Dubovik, O., Fuertes, D., Schuster, G., Cachorro, V. E., Lapyonok, T., Goloub, P., Blarel, L., Barreto, A., Mallet, M., Toledano, C., and Tanré, D. Advanced characterisation of aerosol size properties from measurements of spectral optical depth using the GRASP algorithm, *Atmos. Meas. Tech.*, *10*, 3743–3781, https://doi.org/10.5194/amt-10-3743-2017, 2017.

1055   Valenzuela, A., Olmo, F. J., Lyamani, H., Antón, M., Quirantes, A., & Alados-Arboledas, L. (2012a). Aerosol radiative forcing during African desert dust events (2005–2010) over Southeastern

Spain. *Atmos. Chem. Phys.*, *12*(21), 10331–10351. https://doi.org/10.5194/acp-12-10331-2012, 2012.

Valenzuela, A., Olmo, F. J., Lyamani, H., Antón, M., Quirantes, A., & Alados-Arboledas, L. (2012b). Classification of aerosol radiative properties during African desert dust intrusions over southeastern Spain by sector origins and cluster analysis. *J. Geophys. Res.*, *117*(D6). https://doi.org/https://doi.org/10.1029/2011JD016885, 2012.

Valenzuela, A., Olmo, F. J., Lyamani, H., Antón, M., Titos, G., Cazorla, A., & Alados-Arboledas, L. Aerosol scattering and absorption Angström exponents as indicators of dust and dust-free days over Granada (Spain). *Atmos. Res.*, *154*, 1–13. https://doi.org/10.1016/J.ATMOSRES.2014.10.015, 2015.

Volten, H., Muñoz, O., Rol, E., De Haan, J. F., Vassen, W., Hovenier, J. W., Muinonen, K., & Nousiainen, T. Scattering matrices of mineral aerosol particles at 441.6 nm and 632.8 nm. *J. Geophys. Res.*, *106*(D15), 17375–17401. https://doi.org/10.1029/2001JD900068, 2001.

Zhang, X., Dai, C., Wei, H., Liu, J., Li, W., Wu, K., & Zou, S. Optical properties of mineral dust aerosols with non-absorptive coating: A numerical investigation. *J. Quant. Spectrosc. Radiat. Transf.*, *302*, 108564. https://doi.org/10.1016/j.jqsrt.2023.108564, 2023.

Zhang, X., Wei, H., Zou, S., Duan, J., Li, W., & Dai, C. Effect of nitrate coatings on the optical properties of mineral dust particles during the haze aging process. *J. Quant. Spectrosc. Radiat. Transf.*, *277*, 107966. https://doi.org/10.1016/j.jqsrt.2021.107966, 2022.